Journal of Pharmaceutical Analysis 16 (2026) 101608

Contents lists available at ScienceDirect

Journal of Pharmaceutical Analysis

journal homepage: www.elsevier.com/locate/jpa

Original article

Mifepristone ameliorates osteoporosis & hyperlipidemia comorbidity through SPNS3-S1P-S1PR1 axis via regulating BMSCs differentiation

Hao Li [a,b,1], Wanyu Sang [a,b,1], Sihang Fan [c], Changyuan Wang [a], Lu Liu [a], Shan Wang [a], Mozhen Liu [c,*], Huijun Sun [a,b,**]

[a] Academy of Integrative Medicine, Dalian Medical University, Dalian, Liaoning, 116000, China
[b] Department of Clinical Pharmacology, College of Pharmacy, Dalian Medical University, Dalian, Liaoning, 116000, China
[c] Department of Orthopaedics, the First Affiliated Hospital, Dalian Medical University, Dalian, Liaoning, 116000, China

ARTICLE INFO

Article history:
Received 22 October 2025
Received in revised form
14 March 2026
Accepted 15 March 2026
Available online 19 March 2026

Keywords:
Osteoporosis
Hyperlipidaemia
Sphingosine-1-phosphate (S1P)
SPNS3
Mesenchymal stem cells
Mifepristone

ABSTRACT

Osteoporosis (OP) and hyperlipidemia (HLP) are major public health concerns that often coexist in postmenopausal women due to ovarian senescence and metabolic dysregulation. This comorbidity drives bone marrow adipocyte accumulation and impaired osteoblast differentiation, linked to altered mesenchymal stem cell (BMSC) fate, thereby worsening both bone loss and lipid metabolic imbalance. However, the underlying mechanisms remain unclear. The purpose of this study was to identify key regulatory pathways underlying OP–HLP comorbidity and to explore potential therapeutic strategies targeting dysregulated BMSC differentiation. To investigate, we developed a murine OP–HLP comorbidity model by combining ovariectomy with a high-fat diet. BMSCs were induced under osteogenic or adipogenic conditions to assess differentiation patterns, while omics-based bioinformatics identified targets and pathways relevant to OP–HLP. Potential therapeutic agents were then screened virtually and validated experimentally. The results identified the SPNS lysolipid transporter 3 (SPNS3)–sphingosine-1-phosphate (S1P)–S1PR1 axis as a critical regulator of BMSCs differentiation. Mifepristone (MIF), acting as a structural stabilizer of SPNS3, enhanced osteogenic differentiation while inhibiting adipogenesis *in vitro*. *In vivo*, MIF significantly improved bone formation and reduced marrow adiposity in OP–HLP mice. In conclusion, this study highlighted the SPNS3–S1P–S1PR1 axis as a novel therapeutic target and suggested repurposing MIF for treating OP–HLP comorbidity. This study provides mechanistic insight into bone-lipid crosstalk and opens opportunities for improved intervention strategies.
© 2026 The Authors. Published by Elsevier B.V. on behalf of Xi'an Jiaotong University. This is an open access article under the CC BY-NC-ND license (http://creativecommons.org/licenses/by-nc-nd/4.0/).

1. Introduction

Osteoporosis (OP) is a prevalent age-related skeletal disorder characterized by reduced bone density, deterioration of bone microarchitecture, and increased fracture risk [1]. Globally, an estimated 200 million individuals are affected by OP [2], with its economic, social, and clinical burden expected to rise alongside the aging population, particularly in Asia [3]. Aging or estrogen deficiency induced OP, such as postmenopausal osteoporosis (PMOP), is characterized by decreased bone mass and the accumulation of adipocytes in the bone marrow cavity [4]. This disruption of the bone microenvironment results from the altered differentiation fate of bone marrow mesenchymal stem cells (BMSCs), shifting from osteoblasts to adipocytes [4]. In the bone marrow, BMSCs act as the common progenitors of fat tissue and bone tissue, and can differentiate into osteoblasts, adipocytes and chondrocytes, apart from other cell phenotypes [5].

In humans, postmenopausal status is associated with an increased prevalence of obesity due to changes in energy metabolism [6]. In elderly postmenopausal female bone marrow, the accumulation of bone marrow adipocytes (BMAds), driven by the imbalance in BMSCs differentiation, compromises bone homeostasis and increases the risk of OP [7]. The National Health and Nutrition Examination Survey III (NHANES III) reports that 63% of

Peer review under responsibility of Xi'an Jiaotong University.
* Corresponding author.
** Corresponding author. Department of Clinical Pharmacology, College of Pharmacy, Dalian Medical University, Dalian, Liaoning, 116044, China.
E-mail addresses: mozhenliu@dmu.edu.cn (M. Liu), sunhuijun@dmu.edu.cn (H. Sun).
[1] Both authors contributed equally to this work.

https://doi.org/10.1016/j.jpha.2026.101608
2095-1779/© 2026 The Authors. Published by Elsevier B.V. on behalf of Xi'an Jiaotong University. This is an open access article under the CC BY-NC-ND license (http://creativecommons.org/licenses/by-nc-nd/4.0/).

individuals with OP also have hyperlipidemia (HLP) [8]. HLP, as another aging-associated metabolic disorder, is characterized by elevated serum lipid levels, including triglycerides (TG), total cholesterol (T-CHO), and elevated lipoproteins, such as low-density lipoprotein cholesterol (LDL-C) [9]. HLP induced accumulation of lipid and lipid oxidation products will not only accumulate in the subendothelial spaces of the vasculature but also in bone tissues [8]. This accumulation is associated with an increase in adipocytes and a reduction in bone-forming related cells (BMSCs, osteoblasts, osteoclasts, osteocytes, etc.) [10]. High-fat diet-induced HLP, which raises serum lipid and lipoprotein levels, is known to impair osteogenesis and accelerate bone loss [11], with HLP-induced OP being characterized by increased bone marrow adiposity [12]. In mammals, bone marrow is the only tissue where adipocytes directly interact with bone tissue [12], where BMSCs play critical roles in maintaining the balance between osteoblastic bone formation and adipogenic marrow fat accumulation [13].

HLP combined with estrogen deficiency will cause BMAds to expand and accelerate cellular aging in the bone and bone marrow microenvironment, leading to impaired bone formation and decreased bone mass [14]. Previous studies have primarily focused on the differentiation imbalance of BMSCs and its role in bone loss, particularly the shift in differentiation from osteoblasts to adipocytes, driven by intrinsic aging or damage to BMSCs [15]. However, the impact of extracellular environment, such as the serum metabolic environment on BMSCs differentiation, particularly the role of circulating lipids (such as the sphingosines), remains poorly understood. Therefore, investigating the effects of lipid-related mediators in serum on BMSCs differentiation is crucial to further elucidate their role in bone homeostasis.

Sphingosine-1-phosphate (S1P), belongs to the sphingosines, is a lipid mediator synthesized intracellularly and released into plasma, lymph, and extracellular fluids. Through its specific receptors, extracellular S1P elicits diverse cellular responses and has been implicated in various physiological and pathological processes, including immunity, allergy, and cancer [16,17]. Recent studies have also highlighted a potential link between S1P and bone loss, as well as OP [18–20]. Data from the Study of Health in Pomerania (SHIP)-Trend population-based study in Germany, which included 4091 participants, demonstrated a positive association between serum S1P levels and markers of bone formation [21]. In our research, analysis of serum lipids in the OP&HLP comorbidity model mice compared with the control mice revealed a positive correlation between S1P and osteogenesis-related osteopontin (OPN) in the bone tissue, alongside a negative correlation between S1P and adipogenesis-related marker peroxisome proliferator-activated receptor gamma (PPARγ). These results enlighten that proteins participate in the synthesis and transport of S1P and receptors of S1P may associate with the OP&HLP comorbidity.

Endocrine disorders and metabolic syndrome resulting from estrogen deficiency in elderly postmenopausal women are frequently accompanied by obesity and HLP. This constellation of factors contributes to a significantly higher incidence of OP in postmenopausal women compared to younger women or male counterparts [14]. To replicate this condition, we developed a mouse model of OP&HLP comorbidity by inducing estrogen deficiency through ovariectomy (OVX) and HLP through a high-fat diet (HFD). This OP and HLP comorbidity model exhibited significantly reduced bone mass along with an increase in serum T-CHO and LDL-C levels compared to mice subjected to either OVX or HFD alone. Meanwhile, the OVX&HFD mice exhibited the phenotype of dysglycemia. The above phenomena indicated that the OVX&HFD model can successfully simulate not only the phenotypes of OP&HLP comorbidity, but also the phenotypes of metabolic syndrome.

Serum lipid-regulating drugs, such as statins, have been shown to prevent clinical bone loss and fracture risk by reducing T-CHO and LDL-C levels [22,23]. However, high doses of statins are associated with significant adverse effects, including liver dysfunction, myalgia, and allergic reactions, while long-term use might exacerbate the risk of new-onset osteoporosis [9,23–25]. Besides, estrogen (E2) therapy for PMOP has been shown to reduce levels of T-CHO and LDL-C [26], but long term use of E2 may increase the risk of neoplastic disease [27]. Thus, the development of more effective drugs against OP&HLP comorbidity with fewer side effects, particularly targeting serum lipid regulation, is urgently needed. Achieving this goal requires a deeper understanding of the mechanisms governing the adipogenic and osteogenic differentiation of BMSCs.

In this study, we conducted a comprehensive investigation to identify genes associated with OP&HLP comorbidity using RNA-sequencing (RNA-seq) datasets from human and mouse samples. Our analysis identified SPNS lysolipid transporter 3 (SPNS3), a S1P transport protein, as a critical gene linked to both OP and HLP. Additionally, we identified POU class 2 homeobox 2 (POU2F2) as another key regulator and, for the first time, experimentally confirmed a novel transcriptional regulatory relationship between the POU2F2 protein and the *SPNS3* gene. Further experiments demonstrated that SPNS3 promotes the osteogenic differentiation of BMSCs while inhibiting their adipogenic differentiation through activation of S1PR1 and via influencing downstream pathways including the mitogen-activated protein kinase (MAPK) and the phosphatidylinositol 3′-kinase (PI3K)-protein kinase B (PKB, also known as Akt), thereby delineating a complete signaling axis. Moreover, via a molecular docking based virtual screen assay on an U.S. Food and Drug Administration (US FDA)-approved drug database, the mifepristone (MIF; RU-486) was found to bind to SPNS3, enhancing its stability and facilitating increased extracellular transport of S1P. Both the *in vitro* and *in vivo* studies revealed that MIF significantly inhibited bone loss, regulated serum lipids, and promoted the osteogenic differentiation of BMSCs. Collectively, our findings not only suggest that MIF holds promise as a therapeutic agent but also reveal that the newly identified POU2F2−SPNS3−S1P−S1PR1 axis represents a novel and mechanistically-grounded therapeutic strategy for managing OP&HLP comorbidity.

2. Methods

2.1. Cell culture and preparation

BMSCs were obtained from HAKATA Company (Cat. No.: M015; Shanghai, China), and mycoplasma screening was performed quarterly. Cells were maintained in Dulbecco's modified Eagle medium/nutrient mixture F-12 (DMEM/F12) medium (Cat. No.: KGM12500NH-500, KeyGEN BioTECH, Nanjing, China) supplemented with 10% fetal bovine serum (FBS; Cat. No.: KGY008, KeyGEN BioTECH, Nanjing, China) and 1% penicillin-streptomycin (100X; Cat. No.: KGY0023, KeyGEN BioTECH, Nanjing, China) under a 5% CO_2 atmosphere at 37 °C. Cultures were kept in the logarithmic growth phase and experiments were conducted using cells with fewer than six passages. Isolation and characterization of primary BMSCs from mouse femurs followed established protocols [28]. The three-line differentiation ability (osteogenic differentiation, adipogenic differentiation, and chondrogenic differentiation) of BMSCs cell line and primary BMSCs after specific induction were regularly detected to rule out abnormal cell differentiation.

For osteogenic differentiation, both BMSCs and primary BMSCs were cultured in complete DMEM/F12 medium enriched with 50 μM ascorbic acid (Cat. No.: A8101, Solarbio Science&Technology Co., Ltd., Beijing, China), 100 mM sodium β-glycerophosphate (Cat. No.: IG1340, Solarbio Science&Technology Co., Ltd., Beijing, China), and 100 nM dexamethasone (Cat. No.: ID0180, Solarbio Science&Technology Co., Ltd., Beijing, China), with medium renewal every three days. Adipogenic induction in primary BMSCs involved the use of complete DMEM/F12 medium supplemented with 1 μM dexamethasone (Cat. No.: ID0180, Solarbio Science&Technology Co., Ltd., Beijing, China), 10 μg/mL insulin (Cat. No.: I8040, Solarbio Science&Technology Co., Ltd., Beijing, China), 200 μM indomethacin (Cat. No.: II0100, Solarbio Science&Technology Co., Ltd., Beijing, China), and 0.5 mM 3-isobutyl-1-methylxanthine (IBMX; Cat. No.: I8450, Solarbio Science&Technology Co., Ltd., Beijing, China), also refreshed every three days.

2.2. Transfection procedures

BMSCs were transfected with small interfering RNAs (siRNAs) against *S1*pr*1* or *Spns3*, along with corresponding negative controls, or with an overexpression plasmid for *Pou2f2* (Gene Pharma Biotech Co., Ltd., Shanghai, China). Lipofectamin 2000 (Cat. No.: 11668019, Thermo Fisher Scientific, Inc., Waltham, MA, USA) was used following the supplier's recommendations. RNA analyses were performed 24 h post-transfection, whereas protein assays were initiated 48 h after transfection. The sequences are detailed in Table S1.

2.3. Cell viability assessment

Cell viability was evaluated using the Cell Counting Kit-8 (Cat. No.: C0037, Beyotime Biotechnology, Shanghai, China). BMSCs were plated in 96-well plates at a density of approximately 5–10 $\times$ 10^3 cells/mL and allowed to adhere for 24 h before pretreatment with different concentrations of MIF (Cat. No.: M7250, Solarbio Science&Technology Co., Ltd., Beijing, China). Following the treatment, 10 μL of Cell Counting Kit-8 (CCK-8) solution (Cat. No.: C0037, Beyotime Biotechnology, Shanghai, China) was added to each well, and the plates were incubated for 4 h at 37 °C in the dark. Absorbance was recorded at 450 nm, and the untreated controls were normalized to 100% viability.

2.4. Alkaline phosphatase (ALP) staining

BMSCs were plated in 24-well plates until reaching 70%–80% confluence. Osteogenic induction was initiated by replacing the medium with osteogenic differentiation medium. After 14 days of culture, cells were fixed with 4% paraformaldehyde (Cat. No.: P1110, Solarbio Science&Technology Co., Ltd., Beijing, China) for 10 min, washed with phosphate-buffered saline (PBS; Cat. No.: GL2206-500, KeyGEN BioTECH Co., Ltd., Nanjing, China), and stained with an ALP kit (Cat. No.: C3206, Beyotime Biotechnology Co., Ltd., Shanghai, China) at 37 °C for 60 min. The dye was subsequently removed, cells were rinsed with PBS, and images were captured using an inverted microscope (Carl Zeiss Meditec AG, Jena, Germany) employing ZEN microscopy software. Identical protocols were applied to blank slices of murine femur sections using the same kit.

2.5. Alizarin Red S (ARS) staining

For mineralization assessment, BMSCs were induced osteogenically for 3 weeks. After fixation with 4% paraformaldehyde for 10 min and PBS washes, cells were incubated with ARS dye solution (2%, pH 4.2; Cat. No.: G1452, Solarbio Science & Technology Co., Ltd., Beijing, China) for 2 h. Excess dye was removed by washing, and images were acquired under standardized conditions. Calcium deposition was quantified by decolorizing the stained cells in 10% cetylpyridine chloride solution at room temperature for 30 min, with absorbance measured at 562 nm.

2.6. Oil Red O staining

BMSCs underwent adipogenic induction for 3 weeks, and then were stained with Oil Red O (Cat. No.: G1262, Solarbio Science & Technology Co., Ltd., Beijing, China) following the manufacturer's protocol. Images were recorded under an inverted microscope (Carl Zeiss Meditec AG, Jena, Germany) using consistent settings, and lipid accumulation was quantified by decolorizing the stained cells with isopropanol for 30 min and measuring absorbance at 510 nm.

2.7. Boron dipyrromethene (BODIPY) staining

After fixation with 4% paraformaldehyde for 10 min and washing with PBS, the cells were stained with 10 μM BODIPY dye (Cat. No.: CA5090, Solarbio Science & Technology Co., Ltd., Beijing, China). Images were taken using the same inverted microscope, and lipid droplet fluorescence intensity was measured via a multifunctional microplate reader.

2.8. Immunofluorescence assay

BMSCs or femur tissue sections were fixed with 4% paraformaldehyde (G1101, Servicebio, Wuhan, China) for 25 min. Cells were then permeabilized with 0.1% Triton X-100 for 15 min, followed by a blocking step using 1% bovine serum albumin (BSA; Cat. No.: A8020, Solarbio Science & Technology Co., Ltd., Beijing, China) for 1 h at room temperature. Primary antibodies (diluted 1:200) were applied overnight at 4 °C. After washing with PBS, samples were incubated with fluorescently labeled secondary antibodies for 1 h at room temperature in the dark. Cell nuclei were counterstained with 2-(4-amidinophenyl)-6-indolecarbamidine dihydrochloride (DAPI; Cat. No.: C0065, 10 μg/mL, Solarbio, Beijing, China) at 37 °C for 15 min. Following PBS washes, coverslips were mounted with anti-fade medium, and images were captured using a fluorescence microscope (Carl Zeiss, Oberkochen, Germany) with ZEN microscopy software.

2.9. Dual-luciferase reporter assay

The promoter region of *SPNS3* was cloned into the *pGL3* vector (synthesized by Gene Pharma Biotech Co., Ltd., Suzhou, China), and transfection was carried out using Lipofectamine 3000 (Cat. No.: L3000015, Thermo Fisher Scientific, Inc., Waltham, MA, USA). Cells were harvested 24 h post-transfection for luciferase activity determination via a dual luciferase assay kit (Cat. No.: FR201-01-V2, TransGen Biotech Co., Ltd., Beijing, China) with Renilla luciferase serving as an internal control.

2.10. RNA-seq

BMSCs treated with adipogenic induction or si-S1pr1 were processed for total RNA extraction using a total RNA extraction reagent (TRIzol; Cat. No.:15596026, Thermo Fisher Scientific, Inc., Waltham, MA, USA). RNA quality was verified using an Agilent 2100 Bioanalyzer (Agilent Technologies, Santa Clara, CA, USA) and quantified via the ND-2000 spectrophotometer (Thermo Fisher Scientific, Inc., Waltham, MA, USA). Only samples meeting quality

criteria (OD260/280 between 1.8 and 2.2, OD260/230 $\geq$ 2.0, RIN $\geq$6.5, 28S:18S $\geq$ 1.0, and >10 μg RNA) were used for library construction using the TruSeq RNA Sample Preparation Kit (Cat. No.: FC-122-1001, Illumina, San Diego, CA, USA). Messenger RNA was enriched using oligo(dT) beads and fragmented before cDNA synthesis. Libraries, containing 200–300 bp fragments, were amplified for 15 cycles with Phusion DNA polymerase (Cat. No.: S1419S, NEB, Ipswich, MA, USA), quantified with a TBS380 fluorometer (Promega, Sunnyvale, CA, USA), and sequenced on the Illumina NovaSeq 6000 platform (paired-end 150 bp reads; Illumina, San Diego, CA, USA) by Shanghai BIOZERON Co., Ltd (Shanghai, China). Post-processing included quality control with Trimmomatic (v0.36), alignment using HISAT2, and gene quantification by HTSeq. Differential gene expression was analyzed using edgeR (criteria: |log2 (fold change)| > 2 and FDR <0.05) with subsequent enrichment analysis performed on the Metascape database (https://metascape.org/gp/index.html).

2.11. Animal studies

The animal study protocols were reviewed and approved by the Ethics Committee of Dalian Medical University (Approval number: AEE23136).

Forty female C57BL/6 mice of six-week-old were acclimatized in a controlled environment (temperature: 23–25 °C; 12-h light/dark cycle; humidity: 55% ± 5%) with free access to standard chow and water. Mice were then randomly divided into the sham (SHAM) and bilateral ovariectomy (OVX) groups. Under pentobarbital sodium (Cat. No.: MYM_MP0787, Biopike, Inc., Beijing, China) anesthesia (50 mg/kg, 1% intraperitoneally), OVX was performed via a dorsal midline incision, with ovaries excised and the incision sutured; the SHAM group received only fat tissue removal. Five days post-surgery, vaginal smears confirmed successful ovariectomy. In the OVX + high-fat diet (HFD) group, mice were fed a high-fat diet (60 kcal%; Cat. No.: D12492, Leishidiet Inc., Nanjing, China), while in the OVX + HFD + MIF group, MIF was administered subcutaneously every three days (20 mg/kg, dissolved in olive oil). For the OVX + HFD + MIF (20 mg/kg) + AAV-si-Spns3 group, AAV9-mediated *Spns3* knockdown was delivered via tail vein injection one-week post-OVX. The dosage of MIF used in mouse models was based on previous studies [29]. There were 8 mice in each group. After 8 weeks of treatment in the SPF Experimental Animal Center at Dalian Medical University, mice were euthanized, plasma was isolated via centrifugation, and femurs were stored at −80 °C for further analyses. Detailed drug information is provided in Table S2.

2.12. Serum indices

Serum biomarkers, including ALP, Ca^{2+}, ACP, LDL, HDL, T-CHO, TG, glucose, cortisol, and corticosterone, were measured using commercial kits from Nanjing Jiancheng Bioengineering Institute (Nanjing, China). S1P, OPG, and osteocalcin (OCN) levels were assessed by enzyme linked immunosorbent assay kits (COIBO BIO Co., Ltd., Shanghai, China).

2.13. Dynamic bone mineral apposition rate

Mice received an intraperitoneal injection of calcein (30 mg/kg; Cat. No.: C7600, Solarbio Science&Technology Co., Ltd., Beijing, China) 10 days before tissue harvest, followed by a second injection (15 mg/kg) three days prior. Non-decalcified femur sections were prepared and imaged using a fluorescent upright microscope (Carl Zeiss Meditec AG, Jena, Germany) with ZEN microscopy software, and the deposition gap between the calcein labels was measured.

2.14. Preparation of bone extracellular matrix (ECM) hydrogels

ECM powder was generated from fresh porcine femurs (procured early morning from a local market) following Yu et al. [30], with modifications. After removal of soft tissues, femurs were reduced to particles (<0.5 mm), degreased in a trichloro-triethylamine:methanol solution (30:1, by mass) at 4 °C with 300 rpm stirring for 72 h, and decalcified in 0.6 mol/L HCl for 72 h. Subsequent treatments with 2 mmol/L $CaCl_2$ (Cat. No.: C7250, Solarbio Science&Technology Co., Ltd., Beijing, China), 0.5 mmol/L ethylenediaminetetraacetic acid (EDTA; Cat. No.: E8040, Solarbio Science&Technology Co., Ltd., Beijing, China), and 8 mmol/L LiCl (Cat. No.: E8040, Solarbio Science&Technology Co., Ltd., Beijing, China) were performed, with each step lasting 1 h. Particles were rinsed with distilled water, freeze-dried, and processed further to remove residual cellular components by incubating in Tris-HCl (Cat. No.: KGA1507, KeyGEN BioTECH, Nanjing, China) buffer with 1 mmol/L phenylmethanesulfonyl fluoride (PMSF; Cat. No.: P0100, Solarbio Science&Technology Co., Ltd., Beijing, China) and 1% Triton X-100 (Cat. No.: T8200, Solarbio Science&Technology Co., Ltd., Beijing, China) for 72 h. After repeated washing and freeze-drying, the decalcified matrix was finely ground; 1 g of powder was dissolved in 20 mL 0.01 mol/L HCl and combined with 100 mg pepsin (Cat. No.: P8160, Solarbio Science&Technology Co., Ltd., Beijing, China), followed by stirring at 4 °C for 96 h. The pH was neutralized using 0.1 mol/L NaOH, and the final concentration was adjusted to 2.5 g/L with DMEM/F12. The mixture was then incubated at 37 °C for 20 min to form a solid hydrogel, which was stored at 4 °C until use.

2.15. Calvarial defect model

Eight-week-old male C57BL/6 mice were anesthetized and prepared aseptically. Two symmetric, circular defects (3.5 mm diameter) were created in the parietal bone while preserving the dura mater. A 10 μL drop of one of the following was applied to the defect: ECM/BMSCs/MIF composite hydrogel (20 μM MIF), ECM/BMSCs composite hydrogel, or blank hydrogel. After complete solidification of the hydrogel, the incision was sutured and mice were allowed to recover for four weeks before further sampling.

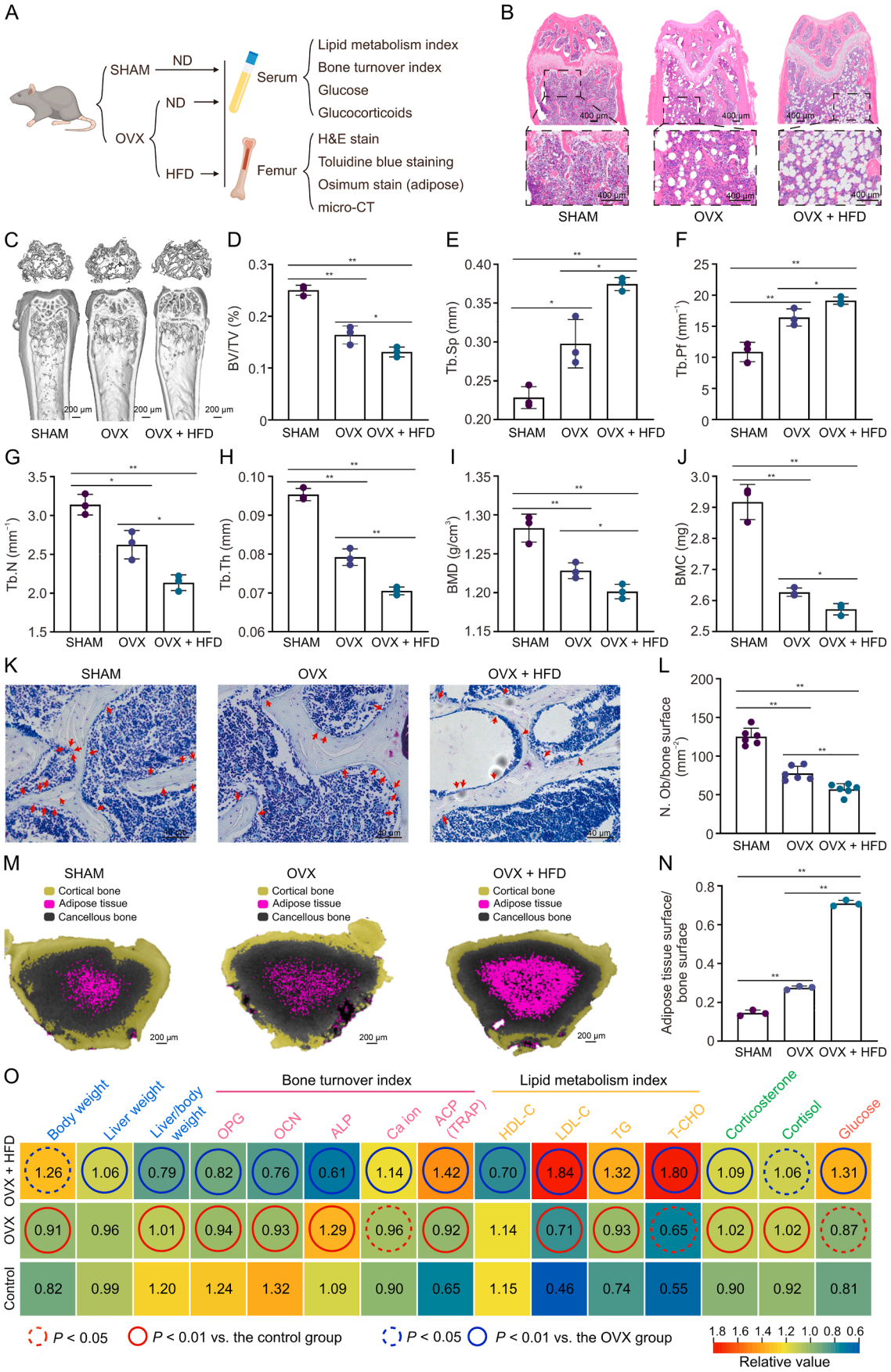
2.16. Histological staining

Hematoxylin and eosin (H&E): Femurs or calvariae were fixed in 4% paraformaldehyde for 72 h, embedded in methyl methacrylate without decalcification, sectioned at 4 μm thickness, and stained with H&E. Imaging was performed using a Carl Zeiss Meditec AG microscope (Carl Zeiss Meditec AG, Jena, Germany).

Toluidine blue staining: Femur slices were stained using a kit from Solarbio Science&Technology Co., Ltd. (Cat. No.: G3668; Beijing, China) following the manufacturer's instructions, and osteoblast quantification was conducted using ImageJ software.

2.17. Micro computed tomography (micro-CT) analysis

Microstructural evaluation of femurs was performed with a Bruker Skyscan 1276 (Bruker Corporation, Billerica, MA, USA). For bone scans, parameters included a voxel size of 6.53 μm, X-ray settings of 70 kV/200 μA with a 0.25 mm aluminum filter, and an integration time of 350 ms. A CaHA phantom was used for density calibration. Analysis was focused on the region spanning the growth plate of the distal femur, covering layers 0 to 100. For adipose tissue imaging, femurs fixed in 4% paraformaldehyde were decalcified in 0.5 mM EDTA (pH 8.0) for 21 days, treated with 1% osmium tetroxide (Cat. No.: 201030, Merck KGaA, Darmstadt,


A
SHAM
ND
OVX
ND
HFD
Serum
Lipid metabolism index
Bone turnover index
Glucose
Glucocorticoids
Femur
H&E stain
Toluidine blue staining
Osimum stain (adipose)
micro-CT
B
SHAM
OVX
OVX + HFD
C
D
BV/TV (%)
E
Tb.Sp (mm)
F
Tb.Pf (mm⁻¹)
G
Tb.N (mm⁻¹)
H
Tb.Th (mm)
I
BMD (g/cm³)
J
BMC (mg)
K
L
N. Ob/bone surface (mm⁻²)
M
Cortical bone
Adipose tissue
Cancellous bone
N
Adipose tissue surface/ bone surface
O
Bone turnover index
Lipid metabolism index
Body weight
Liver weight
Liver/body weight
OPG
OCN
ALP
Ca ion
ACP (TRAP)
HDL-C
LDL-C
TG
T-CHO
Corticosterone
Cortisol
Glucose
OVX + HFD
OVX
Control
1.26 1.06 0.79 0.82 0.76 0.61 1.14 1.42 0.70 1.84 1.32 1.80 1.09 1.06 1.31
0.91 0.96 1.01 0.94 0.93 1.29 0.96 0.92 1.14 0.71 0.93 0.65 1.02 1.02 0.87
0.82 0.99 1.20 1.24 1.32 1.09 0.90 0.65 1.15 0.46 0.74 0.55 0.90 0.92 0.81
P < 0.05
P < 0.01 vs. the control group
P < 0.05
P < 0.01 vs. the OVX group
Relative value

Germany) and 2.5% potassium dichromate (Cat. No.: C0111520275, Nanjing Reagent, Co., Ltd., Nanjing, China) for 3 days, and scanned at 50 kV/60 mA with a resolution of 5 μm. Three-dimensional reconstructions were generated using NRecon (v1.7.4.2).

2.18. Collection of human femoral tissues

The femur tissues were obtained from a cohort of female patients of aged between 30 and 80 undergoing hip replacement surgery. Prior to participation, written informed consent was obtained from each individual, and pertinent demographic and health information, including age, gender, and health status, was documented. Individuals with other metabolic bone diseases, prior treatment with medications affecting bone turnover (e.g., alendronate, and estrogens), or histories of smoking/alcohol consumption were excluded. Bone mineral density (BMD) was measured by dual-energy X-ray absorptiometry to identify the phenotype of OP. These tissues were processed for reverse transcription-quantitative polymerase chain reaction (RT-qPCR) and Western blot (WB) analyses.

The clinical sample experiments in this study strictly adhered to the ethical principles of the Declaration of Helsinki. The use of clinical samples was approved by the Ethics Committee of the First Affiliated Hospital of Dalian Medical University (Approval number: YJ-KY-FB-2023-14). Informed consent was obtained from all participants involved in this study, and written consent was also secured for the publication of the findings. We gratefully acknowledge the voluntary cooperation of all individuals, whose contributions have been invaluable in advancing scientific knowledge in this field.

2.19. RT-qPCR analysis

Total RNA was isolated from cultured cells or femur tissues using the EasyPure® RNA Kit (ER101-01, TransGen Biotech Co., Ltd., Beijing, China), followed by reverse transcription into cDNA using the gDNA Removal and cDNA Synthesis SuperMix (Cat. No.: AU341-02-V2, TransGen Biotech Co., Ltd., Beijing, China). RNA concentrations were determined spectrophotometrically (OD260/280), and primers (designed using Primer Premier 5.5 and synthesized by Sangon Biotech, Shanghai, China) are listed in Table S3. RT-qPCR was performed with TransStart Top Green qPCR SuperMix (Cat. No.: AQ131-01, TransGen Biotech Co., Ltd., Beijing, China) on a Bio-Rad Real-Time PCR System (Bio-Rad Laboratories, Inc., Hercules, CA, USA), and relative gene expression was calculated using the $2^{-\Delta\Delta Ct}$ method.

2.20. WB analysis

Cells or femur tissues were homogenized and proteins extracted using lysis buffer (Cat. No.: P0013J, Beyotime Biotechnology, Shanghai, China). Protein concentrations were measured using a bicinchoninic acid (BCA) kit (Cat. No.: PC0020, Solarbio Science&Technology Co., Ltd., Beijing, China). Proteins (equal loads) were separated by 10%–12% sodium dodecyl sulfate polyacrylamide gel electrophoresis (SDS-PAGE), transferred to polyvinylidene fluoride (PVDF) membranes (Cat. No.: FFP24, Beyotime Biotechnology, Shanghai, China), blocked with skim milk for 2 h, and incubated with primary antibodies overnight at 4 °C. Following incubation with secondary antibodies at 37 °C for 1 h, protein bands were visualized using enhanced chemiluminescence (ECL) reagent (Cat. No.: PE0010, Solarbio Science&Technology Co., Ltd., Beijing, China) and quantified with a luminescence imaging system (Tianneng Life Science, Shanghai, China). Antibodies used are detailed in Table S4.

2.21. Cellular thermal shift assay (CETSA)

Briefly, following treatment with MIF or dimethyl sulfoxide (DMSO; Cat. No.: 3869, Tianjin Damao Chemical Reagent Partnership Enterprise, Tianjin, China) control, cells were exposed to heat challenges at temperatures of 40, 45, 50, 55, and 60 °C, or treated with variable doses of MIF at a constant 60 °C. Protein thermal stability was then determined by WB analysis.

2.22. Cycloheximide (CHX) chase and pronase E stability assays

BMSCs seeded at 1×10^5 cells per well in 6-well plates were treated with varying concentrations of MIF, CHX, or pronase E. To examine the relative expression of SPNS3, cells were harvested at the designated time points, lysed, and subjected to WB analysis for protein level quantification.

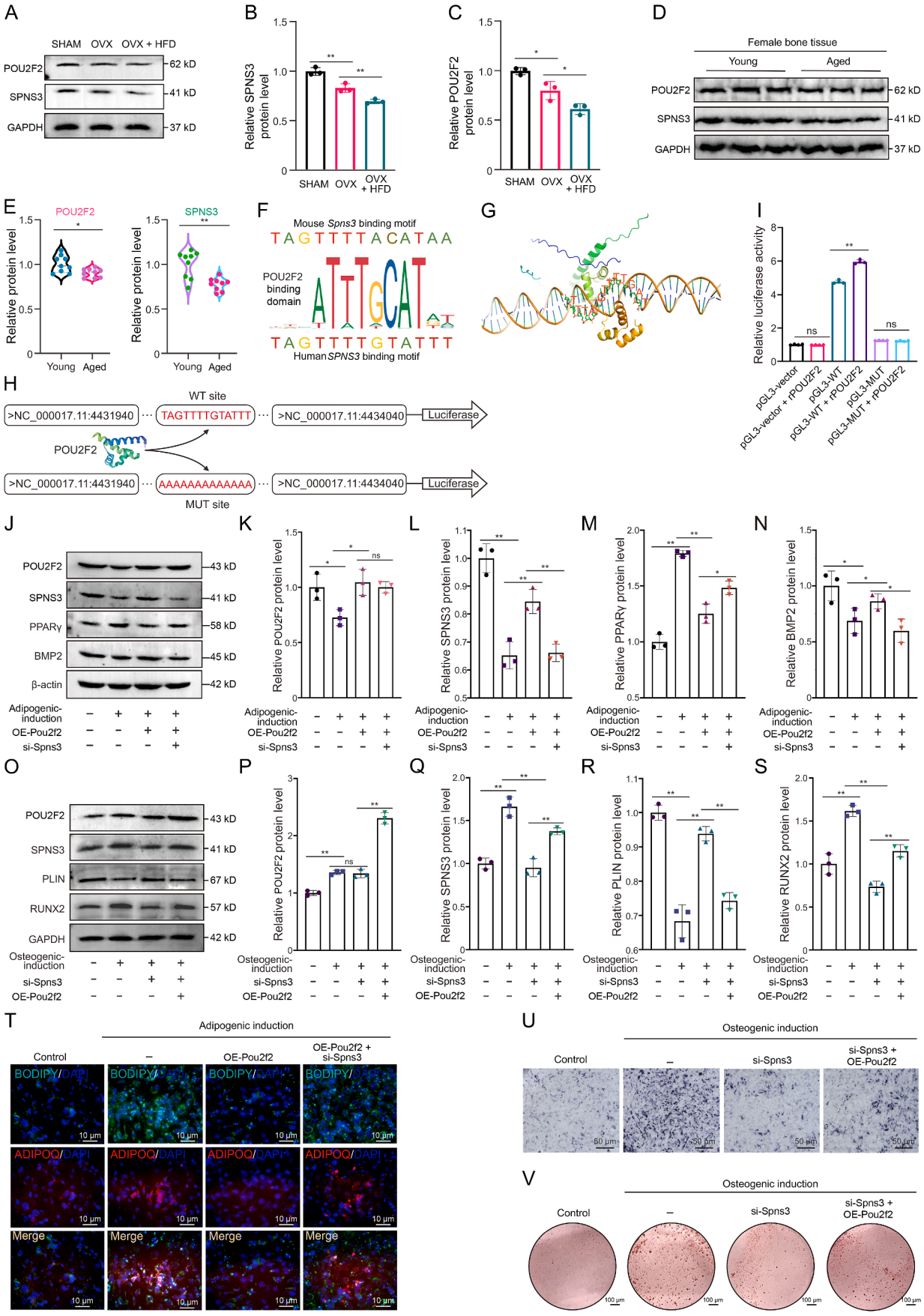
2.23. Molecular docking and virtual screening

The three-dimensional structure of SPNS3 was generated using AlphaFold (https://alphafold.ebi.ac.uk/), while S1PR1 was sourced from the RCSB PDB (https://www.rcsb.org/). Two-dimensional structure files (.SDF) for US FDA-approved drugs were obtained from the ZINC database (https://zinc12.docking.org/). Receptor dehydration was carried out in PyMOL, and Autodock Vina was employed for hydrogenation, charge calculation, and docking of proteins with ligands. The binding sites were defined based on typical S1P active pockets, and the docking results were visualized using PyMOL and the Proteins Plus online tool (http://proteins.plus). In addition, docking studies between POU2F2 and the *SPNS3* gene promoter were conducted using the AlphaFold3 Server (https://deepmind.google/), the docking result was used to guide subsequent experimental design.

2.24. Molecular dynamics simulation

Molecular dynamics (MD) simulations were run using GROMACS (v2022.3) to validate the SPNS3-MIF complex from docking studies. Simulations were conducted under constant temperature (300 K) and pressure (1 bar), employing the Amber99sb-ildn force field and Tip3p water model. Ions (Na^+/Cl^-) were added to neutralize the system, followed by energy minimization via the steepest descent method and equilibration in NVT (canonical ensemble; N: number of particles; V: volume; T: temperature) and NPT (isothermal-isobaric ensemble; N: number of particles; P: pressure; T: temperature) ensembles (each for 100 ps, 100,000 steps). A production run of 100 ns (5,000,000 steps) was performed, and the trajectory data were analyzed by calculating the

Fig. 1. High fat diet aggravates estrogen deficiency induced osteoporosis (OP). (A) Schema of animal experimental design. (B) Hematoxylin-eosin (H&E) staining assay of mice femurs. $n = 3$ (independent biological replicates, the same as below). (C–J) Micro computed tomography (micro-CT) of mice femurs (C) and bone mass related parameters: bone volume/tissue volume (BV/TV) (D), trabecular separation (Tb. Sp) (E), trabecular pattern factor (Tb. Pf) (F), trabecular number (Tb. N) (G), trabecular thickness (Tb.Th) (H), bone mineral density (BMD) (I), and bone mineral content (BMC) (J). $n = 3$, $^{**}P < 0.01$, $^{*}P < 0.05$. (K, L) Toluidine blue staining for osteoblast counting (K) and quantitative analysis (L). $n = 6$, $^{**}P < 0.01$. (M, N) Osmium ion staining for femur fat tissues assay (M) and quantitative analysis (N). $n = 3$, $^{**}P < 0.01$. (O) Heatmap of mouse model related parameters. $n = 4$. OPG: osteoprotegerin; OCN: osteocalcin; ALP: alkaline phosphatase; ACP: acid phosphatase; TRAP: tartrate resistant acid phosphatase; TG: total triglyceride; T-CHO: total cholesterol; HDL-C: high-density lipoprotein cholesterol; LDL-C: low-density lipoprotein; SHAM: sham-operated; OVX: ovariectomized; HFD: high fat diet.


A
SHAM OVX OVX + HFD
POU2F2
SPNS3
GAPDH
62 kD
41 kD
37 kD
B
Relative SPNS3 protein level
SHAM OVX OVX + HFD
C
Relative POU2F2 protein level
SHAM OVX OVX + HFD
D
Female bone tissue
Young
Aged
POU2F2
SPNS3
GAPDH
62 kD
41 kD
37 kD
E
POU2F2
SPNS3
Relative protein level
Young Aged
F
Mouse Spns3 binding motif
TAGTTTTACATAA
POU2F2 binding domain
TAGTTTTGTATTT
Human SPNS3 binding motif
G
I
Relative luciferase activity
ns
pGL3-vector
pGL3-vector + rPOU2F2
pGL3-WT
pGL3-WT + rPOU2F2
pGL3-MUT
pGL3-MUT + rPOU2F2
H
WT site
>NC_000017.11:4431940
TAGTTTTGTATTT
>NC_000017.11:4434040
Luciferase
POU2F2
>NC_000017.11:4431940
AAAAAAAAAAAAA
>NC_000017.11:4434040
Luciferase
MUT site
J
POU2F2
SPNS3
PPARγ
BMP2
β-actin
43 kD
41 kD
58 kD
45 kD
42 kD
Adipogenic-induction
OE-Pou2f2
si-Spns3
K
Relative POU2F2 protein level
L
Relative SPNS3 protein level
M
Relative PPARγ protein level
N
Relative BMP2 protein level
O
POU2F2
SPNS3
PLIN
RUNX2
GAPDH
43 kD
41 kD
67 kD
57 kD
42 kD
Osteogenic-induction
si-Spns3
OE-Pou2f2
P
Relative POU2F2 protein level
Q
Relative SPNS3 protein level
R
Relative PLIN protein level
S
Relative RUNX2 protein level
T
Adipogenic induction
Control
–
OE-Pou2f2
OE-Pou2f2 + si-Spns3
BODIPY/DAPI
ADIPOQ/DAPI
Merge
10 μm
U
Osteogenic induction
Control
–
si-Spns3
si-Spns3 + OE-Pou2f2
50 μm
V
Osteogenic induction
Control
–
si-Spns3
si-Spns3 + OE-Pou2f2
100 μm

root-mean-square deviation (RMSD) of amino acids to assess structural stability.

2.25. Statistical analysis

Data is presented as means ± standard deviation (SD). Statistical tests and graph generation were performed using GraphPad Prism 7.0. For two-group comparisons, a Student's *t*-test was used; for more than two groups, one-way analysis of variance (ANOVA) followed by Tukey's post-hoc test was applied. Statistical significance was set at $^{*}P < 0.05$ and $^{**}P < 0.01$. The "*n*" of biological experiments in this study means independent biological replicates.

3. Results

3.1. OP&HLP comorbidity exacerbates bone loss caused by E2 deficiency

To simulate the clinical features of OP&HLP comorbidity, an OVX&HFD mouse model was established (Fig. 1A). As illustrated in Fig. 1B, the femurs of OVX&HFD mice displayed more pronounced cavities compared to the SHAM group and OVX group, primarily attributed to an increase in adipocytes. Micro-CT analysis revealed a significant reduction in bone mass, trabecular density, and cortical bone thickness in OVX&HFD mice (Figs. 1C–J). Furthermore, the number of osteoblasts on the trabecular surface was markedly reduced in these mice (Figs. 1K and L). In contrast, bone marrow adiposity was significantly elevated in the OVX&HFD group (Figs. 1M and N). Serum metabolic assessments demonstrated a decline in bone formation markers accompanied by an increase in lipid metabolism markers (Fig. 1O). Additionally, body weight, liver weight, glucocorticoid levels, and glucose levels, combined with lipid metabolism index were notably elevated in OVX&HFD mice, while bone formation index was decreased (Figs. 1O and S1). Collectively, these findings indicate that the OVX&HFD mice developed a phenotype and metabolic syndrome consistent with OP&HLP comorbidity.

3.2. Identification of OP related genes and HLP related genes

Having established a reliable animal model, we next sought to identify the key molecular drivers behind the OP&HLP comorbidity phenotype. To identify genes associated with OP&HLP comorbidity, a comprehensive public RNA-seq-based bioinformatics approach was employed (the specific sample information is shown in Table S5), integrating machine learning verification and experimental validation (Fig. S2), and the results are shown in Figs. S3–S5. Firstly, OP-related genes were identified using the Gene Expression Omnibus 2 R (GEO2R) tool to extract differentially expressed genes (DEGs) (Figs. S3A and S4A), complemented by weighted gene co-expression network analysis (WGCNA) to pinpoint modules most strongly correlated with OP (Figs. S3B, S3C, and S4B–G). A Venn diagram analysis (Fig. S3D) revealed 125 OP-associated genes from the intersection of DEGs identified by GEO2R (325 genes) and WGCNA (304 genes).

Next, a similar methodology was applied to identify HLP-related genes (Figs. S3E–I and S5). The intersection of HLP-related genes derived from Limma analysis (325 genes) and WGCNA (3 modules) is shown in Fig. S3J. Unlike the analysis for OP-related genes, a significant mismatch was observed between genes identified by Limma and WGCNA for HLP. Consequently, the subsequent analyses incorporated the union of these gene sets, rather than the intersection of these gene sets.

The overlap between HLP and OP-associated genes is illustrated through an upset diagram (Fig. S3K). Next, these overlapping genes were selected and subjected to the next round of enrichment analysis as well as further screening using machine learning algorithms (Figs. S6 and S7). 34 shared genes were ultimately identified (Figs. S6A and B). Enrichment analysis of these genes revealed significant associations with steroid hormone-related pathways, the MAPK pathway (Fig. S6C), and other pathways known to play critical roles in both OP and HLP pathogenesis.

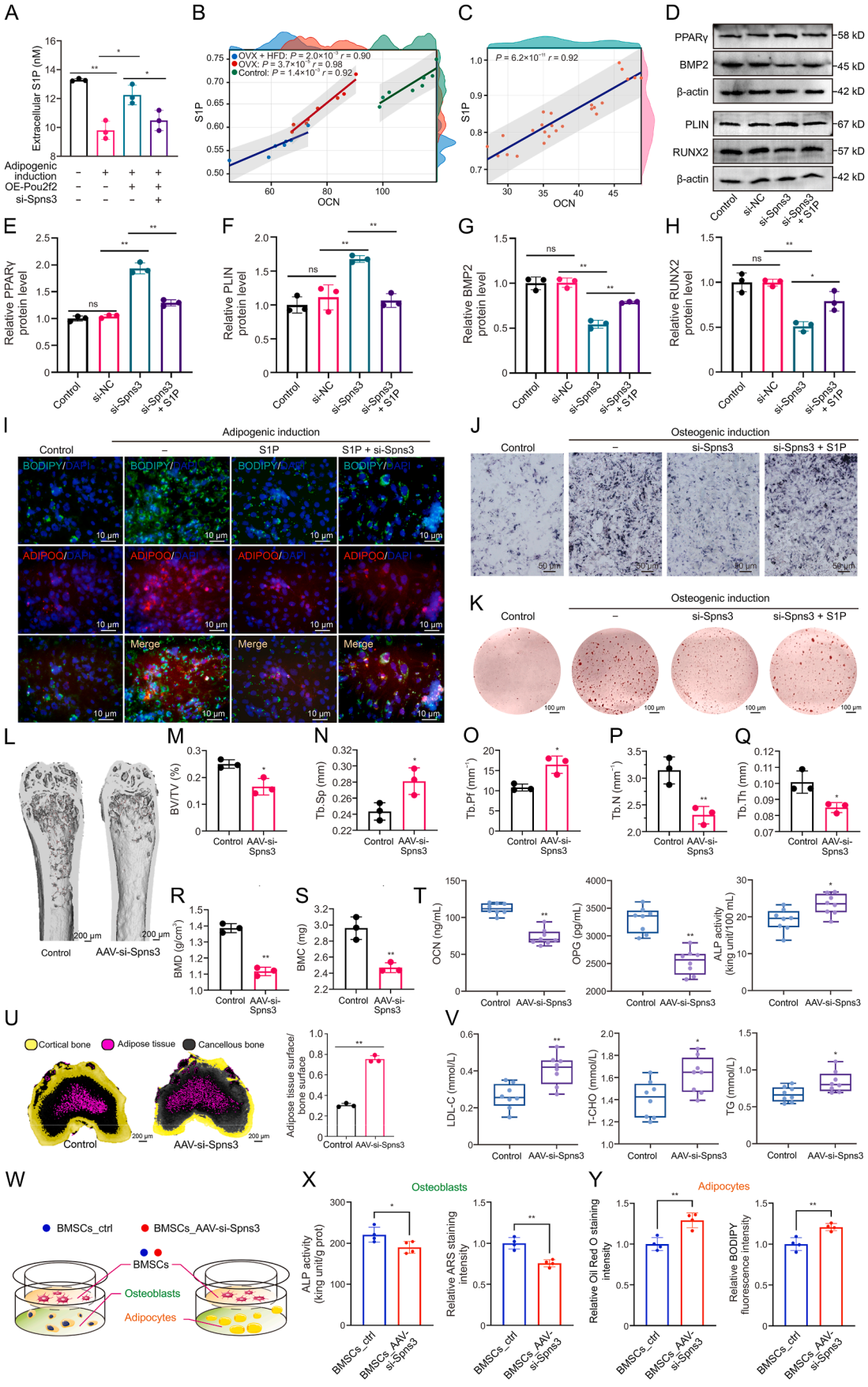
3.3. Identification of OP&HLP comorbidity related genes

To refine this candidate gene list and prioritize the most robust targets for experimental validation, machine learning models were employed. Least absolute shrinkage and selection operator (LASSO) regression and Random Forest were selected, for their complementary strengths in handling high-dimensional genomic data. LASSO provides effective feature selection by shrinking irrelevant gene coefficients to zero, while Random Forest robustly captures complex, non-linear relationships and provides variable importance metrics [31,32].

First, the expression profile data of the 34 candidate genes identified in Fig. S7A (red numbers) was used as input for further analysis. LASSO regression was applied to identify potential genes associated with OP&HLP comorbidity. This analysis revealed 11 genes strongly correlated with both conditions (Figs. S7B and C). Next, the Random Forest algorithm was used to refine the selection, filtering out the 7 most significant biomarkers linked to OP&HLP comorbidity (Figs. S7D–F). The intersections of genes identified by LASSO regression and Random Forest are displayed in Figs. S6D and S7G, resulting in the identification of 5 key genes (*ALPL*, *NEDD9*, *MYL10*, *POU2F2*, and *SPNS3*). The relative expression levels of these genes and their receiver operating characteristic (ROC) curves are shown in Figs. S6E and F.

Single-gene gene set enrichment analysis (Single-gene GSEA) of the screened genes based on an RNA-seq array of mesenchymal stem cells from primary OP or healthy human (GSE35959, Table S5) indicated strong associations between lipid metabolism and *POU2F2* gene and *SPNS3* gene (Figs. S7H and I). RT-qPCR analysis of human bone samples confirmed a correlation between POU2F2 and SPNS3 with osteogenic marker OPN and adipogenic marker PPARγ (Figs. S7J–M). Furthermore, expression levels of

Fig. 2. POU class 2 homeobox 2 (POU2F2) transcriptional controls SPNS lysolipid transporter 3 (SPNS3) in bone marrow mesenchymal stromal cells (BMSCs) to regulate the osteogenic/adipogenic balance. (A–C) Western blot (WB) detection (A) and quantitative analysis of SPNS3 (B) and POU2F2 (C) in mice femurs. $n = 3$, $^{**}P < 0.01$, $^{*}P < 0.05$ (independent biological replicates, the same as below). (D, E) WB detection (D) and quantitative analysis (E) of POU2F2 and SPNS3 in human samples. $n = 9$, $^{**}P < 0.01$, $^{*}P < 0.05$. (F) Matchup assay between mouse/human *SPNS3* transcription factor (TF) binding motif and related DNA binding domain of POU2F2. (G) The binding between *SPNS3*'s promoter and POU2F2 protein was verified by AlphaFold 3 server. (H, I) Illustration of dual luciferase reporter analysis (H) and the results indicating that POU2F2 can regulate the promoter activity of SPNS3 (I). $n = 4$, $^{**}P < 0.01$, ns, not significant. (J–N) WB detection (J) was used to detect the influence of POU2F2 (K) and SPNS3 (L) on BMSCs differentiation indicators peroxisome proliferator-activated receptor gamma (PPARγ) (M) and bone morphogenetic protein 2 (BMP2) (N) during adipogenic induction. $n = 3$, $^{**}P < 0.01$, $^{*}P < 0.05$, ns, non-significant. (O–S) WB detection (O) was used to detect the influence of POU2F2 (P) and SPNS3 (Q) on BMSCs differentiation indicators perilipin (PLIN) (R) and runt-related transcription factor 2 (RUNX2) (S) during osteogenic induction. $n = 3$, $^{**}P < 0.01$, ns, not significant. (T) Immunofluorescence (IF) staining of adipogenic differentiation indicator adiponectin (ADIPOQ) and Boron dipyrromethene (BODIPY) staining for detection of lipids, during adipogenic induction of BMSCs. $n = 3$. (U, V) Alkaline phosphatase (ALP) staining (U) and Alizarin Red S (ARS) staining (V) during osteogenic induction of BMSCs. $n = 3$. SHAM: sham-operated; OVX: ovariectomized; HFD: high fat diet; WT: wild type; MUT: mutant type; GAPDH: glyceraldehyde-3-phosphate dehydrogenase.


A
Extracellular S1P (nM)
Adipogenic induction
OE-Pou2f2
si-Spns3
B
OVX + HFD: P = 2.0×10⁻³ r = 0.90
OVX: P = 3.7×10⁻³ r = 0.98
Control: P = 1.4×10⁻³ r = 0.92
S1P
OCN
C
P = 6.2×10⁻¹¹ r = 0.92
S1P
OCN
D
PPARγ
BMP2
β-actin
PLIN
RUNX2
β-actin
58 kD
45 kD
42 kD
67 kD
57 kD
42 kD
Control
si-NC
si-Spns3
si-Spns3 + S1P
E
Relative PPARγ protein level
F
Relative PLIN protein level
G
Relative BMP2 protein level
H
Relative RUNX2 protein level
I
Adipogenic induction
Control
–
S1P
S1P + si-Spns3
BODIPY/DAPI
ADIPOQ/DAPI
Merge
10 μm
J
Osteogenic induction
Control
–
si-Spns3
si-Spns3 + S1P
50 μm
K
Osteogenic induction
Control
–
si-Spns3
si-Spns3 + S1P
100 μm
L
200 μm
Control
AAV-si-Spns3
M
BV/TV (%)
N
Tb.Sp (mm)
O
Tb.Pf (mm⁻¹)
P
Tb.N (mm⁻¹)
Q
Tb.Th (mm)
R
BMD (g/cm³)
S
BMC (mg)
T
OCN (ng/mL)
OPG (pg/mL)
ALP activity (king unit/100 mL)
U
Cortical bone
Adipose tissue
Cancellous bone
Adipose tissue surface/ bone surface
V
LDL-C (mmol/L)
T-CHO (mmol/L)
TG (mmol/L)
W
BMSCs_ctrl
BMSCs_AAV-si-Spns3
BMSCs
Osteoblasts
Adipocytes
X
Osteoblasts
ALP activity (king unit/g prot)
Relative ARS staining intensity
Y
Adipocytes
Relative Oil Red O staining intensity
Relative BODIPY fluorescence intensity
BMSCs_ctrl
BMSCs_AAV-si-Spns3

POU2F2 gene and *SPNS3* gene in the validation dataset demonstrated significant differences between OP and healthy bone samples in humans (Fig. S8A).

Based on their strong computational association with lipid metabolism and bone phenotypes, POU2F2 and SPNS3 were selected as the lead candidates for further mechanistic investigation.

3.4. POU2F2 transcriptionally controls SPNS3 in BMSCs to regulate the osteogenic/adipogenic differentiation balance

SPNS3, a member of the SPNS lysolipid transporter family, is predicted to function as a transporter of S1P. Compared to its homolog, SPNS2, which has been well-established as an S1P transporter, SPNS3 exhibited significant bone marrow-specific expression (Figs. S8B–E), suggesting that it might play a crucial role in bone development. On the other hand, *POU2F2*, a gene encoding the transcription factor POU2F2, does not display tissue-specific expression (Figs. S8F and G). In the femurs of OVX&HFD mice, a reduction in the protein levels of both SPNS3 and POU2F2 was observed (Figs. 2A–C). Additionally, in bone tissues from elderly individuals with OP and HLP phenotypes (Figs. S9A–D), the expression levels of SPNS3 and POU2F2 were also significantly reduced when compared to those in young control samples (Figs. 2D and E). These findings suggest a potential involvement of SPNS3 and POU2F2 in the pathophysiology of OP&HLP comorbidity.

The role of POU2F2 as a transcription factor and its co-expression tendency with SPNS3 prompted us to hypothesize whether it could regulate the transcription of *SPNS3* gene. Using the transcription factor-binding site prediction tool JASPAR [33], we identified potential binding sites for POU2F2 in the promoter region of the *SPNS3* gene (Fig. 2F). The predicted results indicated that POU2F2 could bind to a conserved sequence within the *SPNS3* promoter region. This interaction was further validated through structural modeling via the AlphaFold 3 server (https://alphafoldserver.com) (Fig. 2G). To experimentally confirm this pivotal interaction, we designed a dual-luciferase reporter assay (Fig. 2H). Overexpression of human POU2F2 significantly enhanced the luciferase activity of the *SPNS3* promoter construct. This result provides strong evidence and definitively confirms the direct transcriptional regulation of *SPNS3* gene by POU2F2 (Fig. 2I).

To evaluate the roles of POU2F2 and SPNS3 in determining the differentiation fate of BMSCs, overexpression of *Pou2f2* gene and silencing of *Spns3* gene were performed during both adipogenic (Figs. 2J–N) and osteogenic differentiation induction (Figs. 2O–S). During adipogenic differentiation, both the expression levels of POU2F2 and SPNS3 exhibited a declining trend (Figs. 2J–L), which correlated with an increase in the adipogenesis-related marker PPARγ and a decrease in the osteogenesis-related marker BMP2 (Figs. 2M and N). Overexpression of *Pou2f2* gene reversed these trends, leading to increased SPNS3 and BMP2 levels while reducing PPARγ expression. However, silencing of *Spns3* gene abolished the effects of *Pou2f2* overexpression, highlighting the interdependence of these proteins (Figs. 2J–N). In osteogenic differentiation, POU2F2 and SPNS3 both demonstrated promotive effects on osteogenesis (Figs. 2O–S). Importantly, silencing *Spns3* gene did not alter the expression of POU2F2 (Figs. 2O, 2P, and S9E–H), establishing POU2F2 as an upstream regulator of SPNS3.

Further functional validation was conducted using BODIPY staining and adiponectin (ADIPOQ) immunofluorescence (IF) staining to visualize lipid droplets during adipogenic differentiation of BMSCs (Fig. 2T). Additionally, ALP staining and ARS staining were employed to assess the effects of POU2F2 and SPNS3 on osteogenic activity of BMSCs (Figs. 2U and V). These experiments hinted the osteogenic-inducing and anti-adipogenic effects mediated by POU2F2 and SPNS3, providing strong evidence for their regulatory roles in BMSCs differentiation.

3.5. SPNS3 regulates osteogenic/adipogenic balance of BMSCs as a S1P transporter

Since SPNS3 is predicted to be an S1P transporter, we investigated whether its function in BMSC differentiation is mediated through S1P signaling. S1P itself has been implicated in the pathophysiology of OP [21]. However, the research on the role of SPNS3, which was initially identified as a transporter of S1P [34,35], remains limited. In the present study, we observed a decrease in extracellular S1P levels during adipogenic differentiation of BMSCs. Notably, overexpression of *Pou2f2* gene led to an increase in extracellular S1P levels, whereas silencing *Spns3* (via si-Spns3) inhibited this effect (Fig. 3A). Furthermore, serum S1P levels were significantly reduced in mice injected with AAV-si-Spns3 compared to control mice (Fig. S9I). Primary BMSCs from AAV-si-Spns3 injected mice also exhibited lower extracellular S1P levels, which was accompanied by decreased osteogenic activity and increased adipogenic differentiation (Figs. S9J–P). These findings suggested that SPNS3-mediated regulation of S1P was critical for maintaining the balance between osteogenesis and adipogenesis in BMSCs. In the mouse model of OP&HLP comorbidity, serum S1P levels were significantly lower compared to the OVX group and the control group. Moreover, serum S1P levels exhibited a positive correlation with the bone formation marker OCN (Fig. 3B). Similar results were observed in human serum samples, where S1P levels were positively associated with indicators of bone formation (Fig. 3C). Instead, serum S1P levels exhibited a negative correlation with the serum lipid indicator T-CHO, both in mice and human samples (Figs. S9Q and R). Importantly, the decrease in osteogenic markers and increase in adipogenic markers caused by *Spns3* gene knockdown in BMSCs were effectively reversed by S1P treatment (Figs. 3D–H), demonstrating that SPNS3 exerts its regulatory role primarily via the production and signaling of S1P. The adipogenic potential of BMSCs was assessed using BODIPY and ADIPOQ IF staining to

Fig. 3. SPNS lysolipid transporter 3 (SPNS3) regulates osteogenic/adipogenic balance of bone marrow mesenchymal stromal cells (BMSCs) as a sphingosine 1-phosphate (S1P) transporter. (A) Detection of extracellular S1P level of BMSCs. $n = 3$, $^{**}P < 0.01$, $^{*}P < 0.05$. (B, C) Mice serum ($n = 8$) (B) and human serum samples ($n = 25$) (C) indicated positive correlation of S1P with osteogenic indicator osteocalcin (OCN). (D–H) Western blot (WB) assay (D) and quantitative analysis of adipogenic differentiation markers peroxisome proliferator-activated receptor gamma (PPARγ) (E) and perilipin (PLIN) (F), and osteogenic differentiation markers bone morphogenetic protein 2 (BMP2) (G) and runt-related transcription factor 2 (RUNX2) (H). $n = 3$, $^{**}P < 0.01$, $^{*}P < 0.05$, ns, not significant (independent biological replicates, the same as below). (I) Immunofluorescence (IF) staining of adipogenic differentiation indicator adiponectin (ADIPOQ) and Boron dipyrromethene (BODIPY) staining for detection of lipids, during adipogenic induction of BMSCs. $n = 3$. (J, K) Alkaline phosphatase (ALP) staining (J) and Alizarin Red S (ARS) staining (K) during osteogenic induction of BMSCs. $n = 3$. (L–S) Micro computed tomography (micro-CT) assay of mice femurs (L) and bone mass related parameters: bone volume/tissue volume (BV/TV) (M), trabecular separation (Tb. Sp) (N), trabecular pattern factor (Tb. Pf) (O), trabecular number (Tb. N) (P), trabecular thickness (Tb.Th) (Q), bone mineral density (BMD) (R), and bone mineral content (BMC) (S). $n = 3$, $^{**}P < 0.01$, $^{*}P < 0.05$. (T) Mice serum bone metabolism parameters. $n = 8$, $^{**}P < 0.01$, $^{*}P < 0.05$. (U) Osmium ion staining for femur fat tissues assay and quantitative analysis. $n = 3$, $^{**}P < 0.01$. (V) Mice serum lipid metabolism parameters. $n = 8$, $^{**}P < 0.01$, $^{*}P < 0.05$. (W) Schematic plot of co-culture BMSCs with osteoblasts/adipocytes. (X) ALP staining and ARS staining of osteoblasts. $n = 4$, $^{**}P < 0.01$, $^{*}P < 0.05$. (Y) Oil Red O staining and BODIPY staining of adipocytes. $n = 4$, $^{**}P < 0.01$. OPG: osteoprotegerin; LDL-C: low-density lipoprotein; T-CHO: total cholesterol; TG: total triglyceride; AAV: adeno-associated virus; NC: negative control; DAPI: 4′,6-diamidino-2-phenylindole.

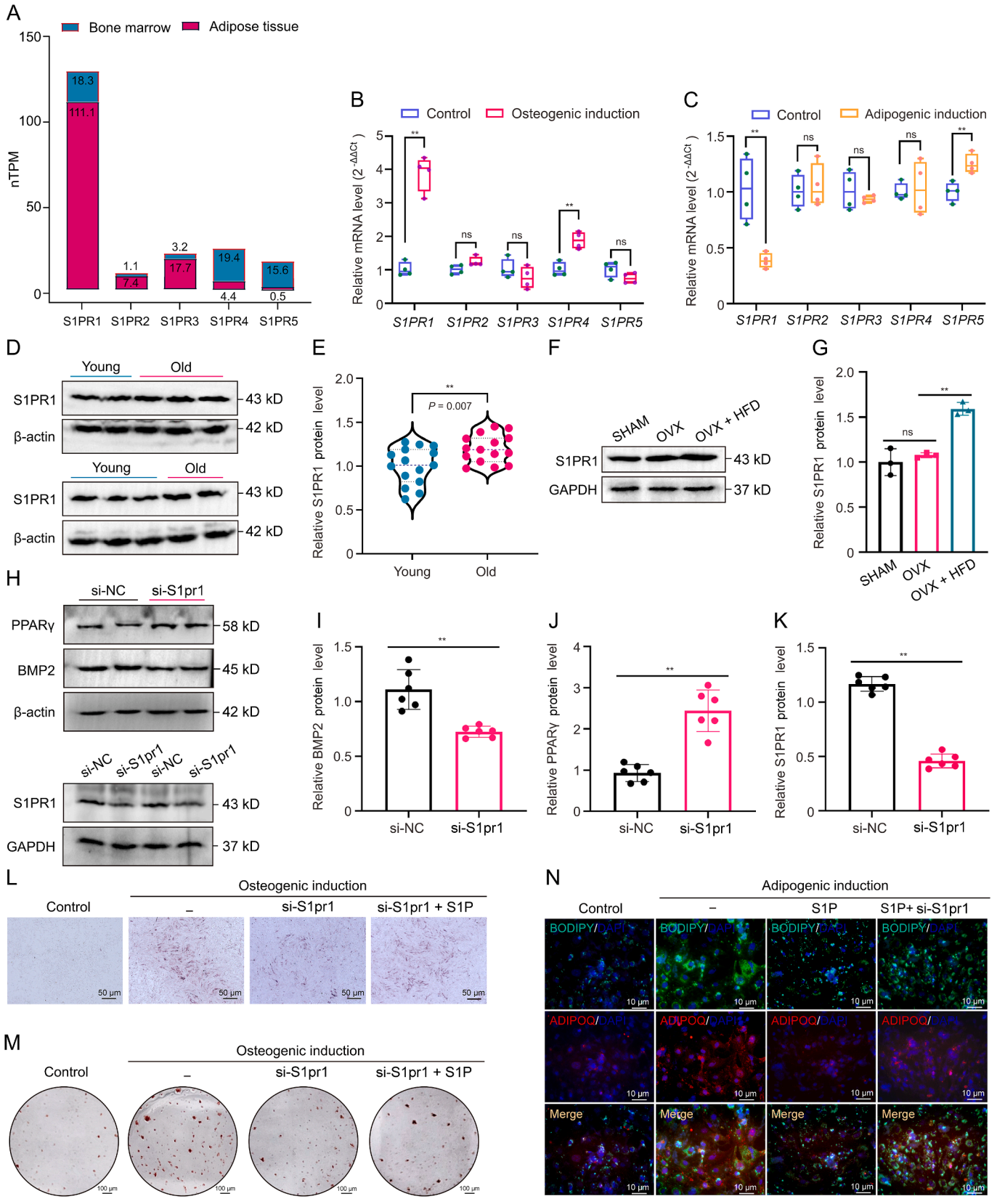


Fig. 4. Sphingosine 1-phosphate (S1P) receptor 1 (S1PR1) regulates osteogenic/adipogenic balance of bone marrow mesenchymal stromal cells (BMSCs). (A) Relative expression levels of S1P receptors 1–5 (S1PRs 1–5) in human bone marrow tissues and adipose tissues. (B, C) Relative expression levels of S1PRs 1–5 during osteogenic differentiation (B) and adipogenic differentiation (C). $n = 4$, $^{**}P < 0.01$; ns, not significant. (D, E) Western blot (WB) detection (D) and quantitative analysis (E) of S1PR1 in human bone tissues. $n = 15$, $^{**}P < 0.01$ (independent biological replicates, the same as below). (F, G) WB detection (F) and quantitative analysis of S1PR1 in mice femurs (G). $n = 3$, $^{**}P < 0.01$, ns, not significant. (H–K) WB detection (H) and quantitative analysis of osteogenic marker bone morphogenetic protein 2 (BMP2) (I) and adipogenesis-related gene peroxisome proliferator-activated receptor gamma (PPARγ) (J) after silencing of S1PR1 (K). $n = 3$, $^{**}P < 0.01$. (L, M) Alkaline phosphatase (ALP) staining (L) and Alizarin Red S (ARS) staining (M) during osteogenic

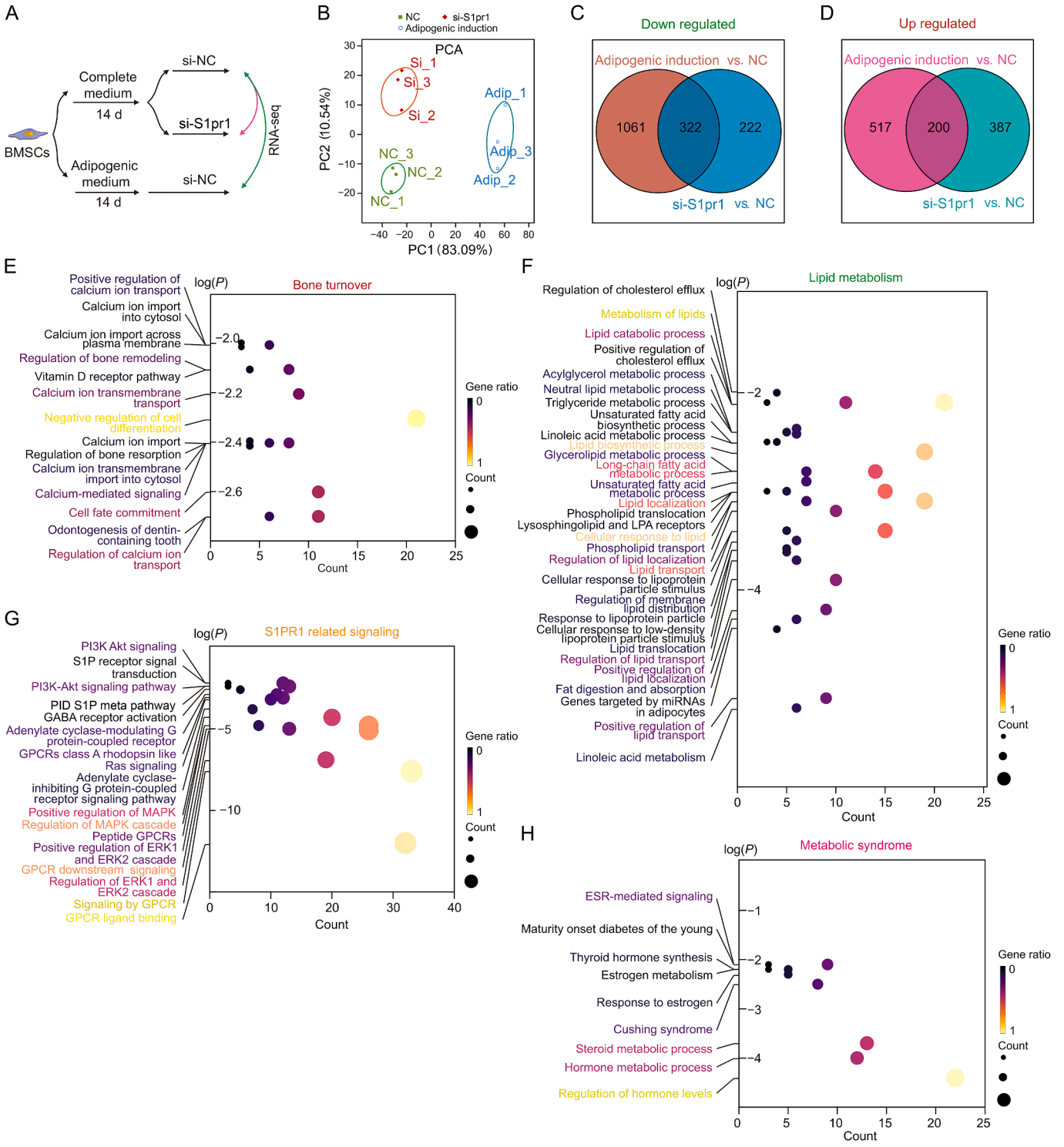
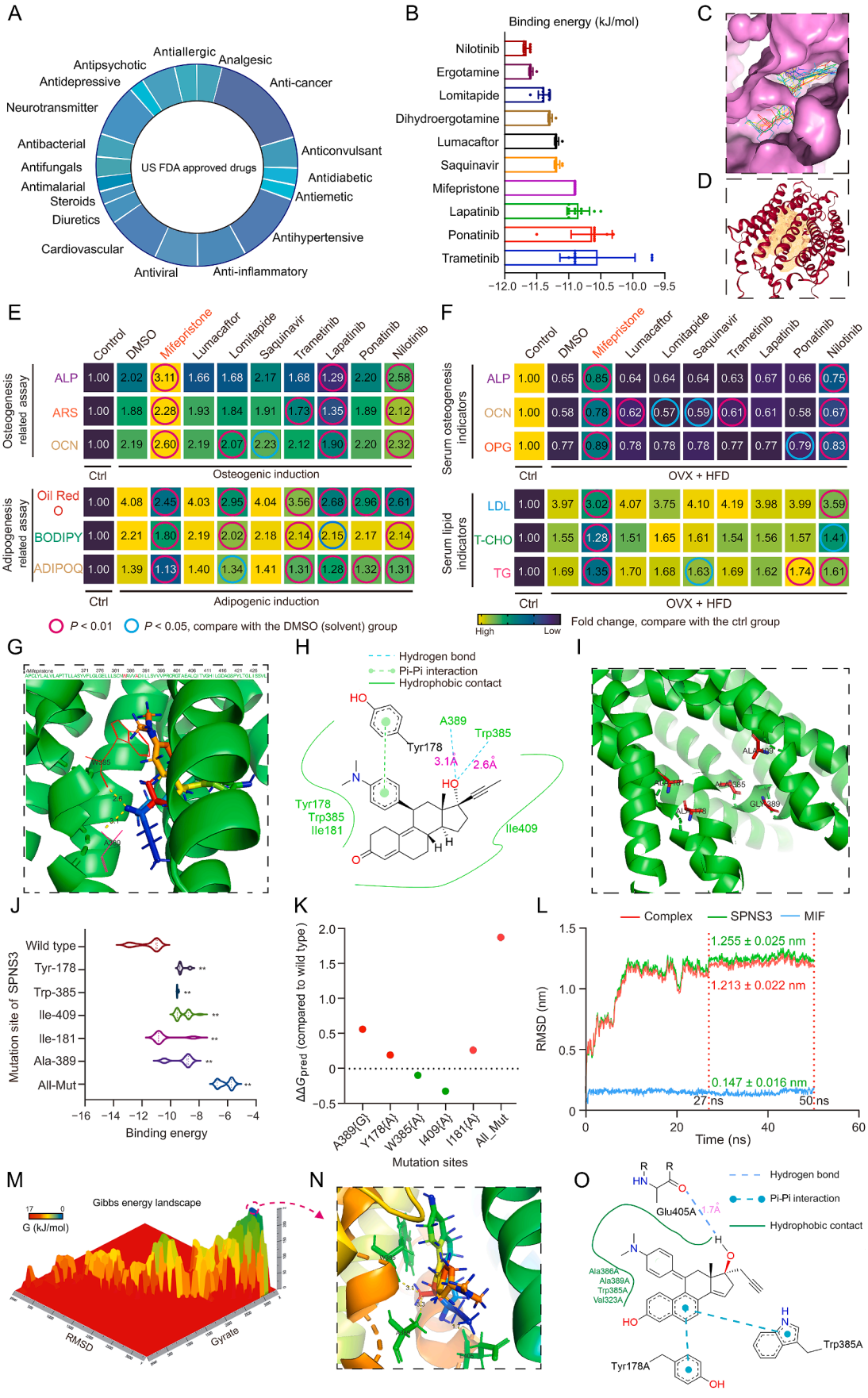


Fig. 5. RNA sequencing (RNA-seq) assay of bone marrow mesenchymal stromal cells (BMSCs). (A) Flowchart of RNA-seq assay on BMSCs. $n = 3$ (independent biological replicates, the same as below). (B) Principal component analysis (PCA) diagram of three groups. (C, D) Venn diagram showing overlapped down-regulating genes (C) or up-regulating genes (D) in three groups. (E–H) Plot diagrams showing results of gene ontology (GO) enrichment analysis from differently expressed genes in three groups: bone turnover related items (E), lipid metabolism related items (F), sphingosine-1-phosphate (S1P) receptor 1 (S1PR1) related signalings (G), and metabolic syndrome related items (H). NC: negative control; Adip: adipogenic induction.

induction of BMSCs. $n = 3$. (N) Immunofluorescence (IF) staining of adipogenic differentiation indicator adiponectin (ADIPOQ) and Boron dipyrromethene (BODIPY) staining for detection of lipids, during adipogenic induction of BMSCs. $n = 3$. SHAM: sham-operated; OVX: ovariectomized; HFD: high fat diet; NC: negative control; DAPI: 4′,6-diamidino-2-phenylindole; GAPDH: glyceraldehyde-3-phosphate dehydrogenase.


A
Antiallergic
Analgesic
Antipsychotic
Antidepressive
Anti-cancer
Neurotransmitter
Antibacterial
Anticonvulsant
Antifungals
Antidiabetic
Antimalarial
Steroids
Antiemetic
Diuretics
Antihypertensive
Cardiovascular
Antiviral
Anti-inflammatory
US FDA approved drugs
B
Binding energy (kJ/mol)
Nilotinib
Ergotamine
Lomitapide
Dihydroergotamine
Lumacaftor
Saquinavir
Mifepristone
Lapatinib
Ponatinib
Trametinib
−12.0 −11.5 −11.0 −10.5 −10.0 −9.5
C
D
E
Control
DMSO
Mifepristone
Lumacaftor
Lomitapide
Saquinavir
Trametinib
Lapatinib
Ponatinib
Nilotinib
Osteogenesis related assay
ALP 1.00 2.02 3.11 1.66 1.68 2.17 1.68 1.29 2.20 2.58
ARS 1.00 1.88 2.28 1.93 1.84 1.91 1.73 1.35 1.89 2.12
OCN 1.00 2.19 2.60 2.19 2.07 2.23 2.12 1.90 2.20 2.32
Ctrl
Osteogenic induction
Adipogenesis related assay
Oil Red O 1.00 4.08 2.45 4.03 2.95 4.04 3.56 2.68 2.96 2.61
BODIPY 1.00 2.21 1.80 2.19 2.02 2.18 2.14 2.15 2.17 2.14
ADIPOQ 1.00 1.39 1.13 1.40 1.34 1.41 1.31 1.28 1.32 1.31
Ctrl
Adipogenic induction
F
Serum osteogenesis indicators
ALP 1.00 0.65 0.85 0.64 0.64 0.64 0.63 0.67 0.66 0.75
OCN 1.00 0.58 0.78 0.62 0.57 0.59 0.61 0.61 0.58 0.67
OPG 1.00 0.77 0.89 0.78 0.78 0.78 0.77 0.77 0.79 0.83
Ctrl
OVX + HFD
Serum lipid indicators
LDL 1.00 3.97 3.02 4.07 3.75 4.10 4.19 3.98 3.99 3.59
T-CHO 1.00 1.55 1.28 1.51 1.65 1.61 1.54 1.56 1.57 1.41
TG 1.00 1.69 1.35 1.70 1.68 1.63 1.69 1.62 1.74 1.61
Ctrl
OVX + HFD
P < 0.01
P < 0.05, compare with the DMSO (solvent) group
High
Low
Fold change, compare with the ctrl group
G
H
Hydrogen bond
Pi-Pi interaction
Hydrophobic contact
HO
A389
Trp385
Tyr178
3.1Å
2.6Å
HO
N
Tyr178
Trp385
Ile181
Ile409
H
O
I
J
Mutation site of SPNS3
Wild type
Tyr-178
Trp-385
Ile-409
Ile-181
Ala-389
All-Mut
−16 −14 −12 −10 −8 −6 −4
Binding energy
K
ΔΔGpred (compared to wild type)
2.0
1.5
1.0
0.5
0
−0.5
A389(G)
Y178(A)
W385(A)
I409(A)
I181(A)
All_Mut
Mutation sites
L
Complex
SPNS3
MIF
RMSD (nm)
1.5
1.0
0.5
0
1.255 ± 0.025 nm
1.213 ± 0.022 nm
0.147 ± 0.016 nm
27 ns
50 ns
0
20
40
60
Time (ns)
M
Gibbs energy landscape
G (kJ/mol)
RMSD
Gyrate
N
O
Hydrogen bond
Pi-Pi interaction
Hydrophobic contact
Glu405A
1.7Å
Ala386A
Ala389A
Trp385A
Val323A
HO
Tyr178A
OH
Trp385A

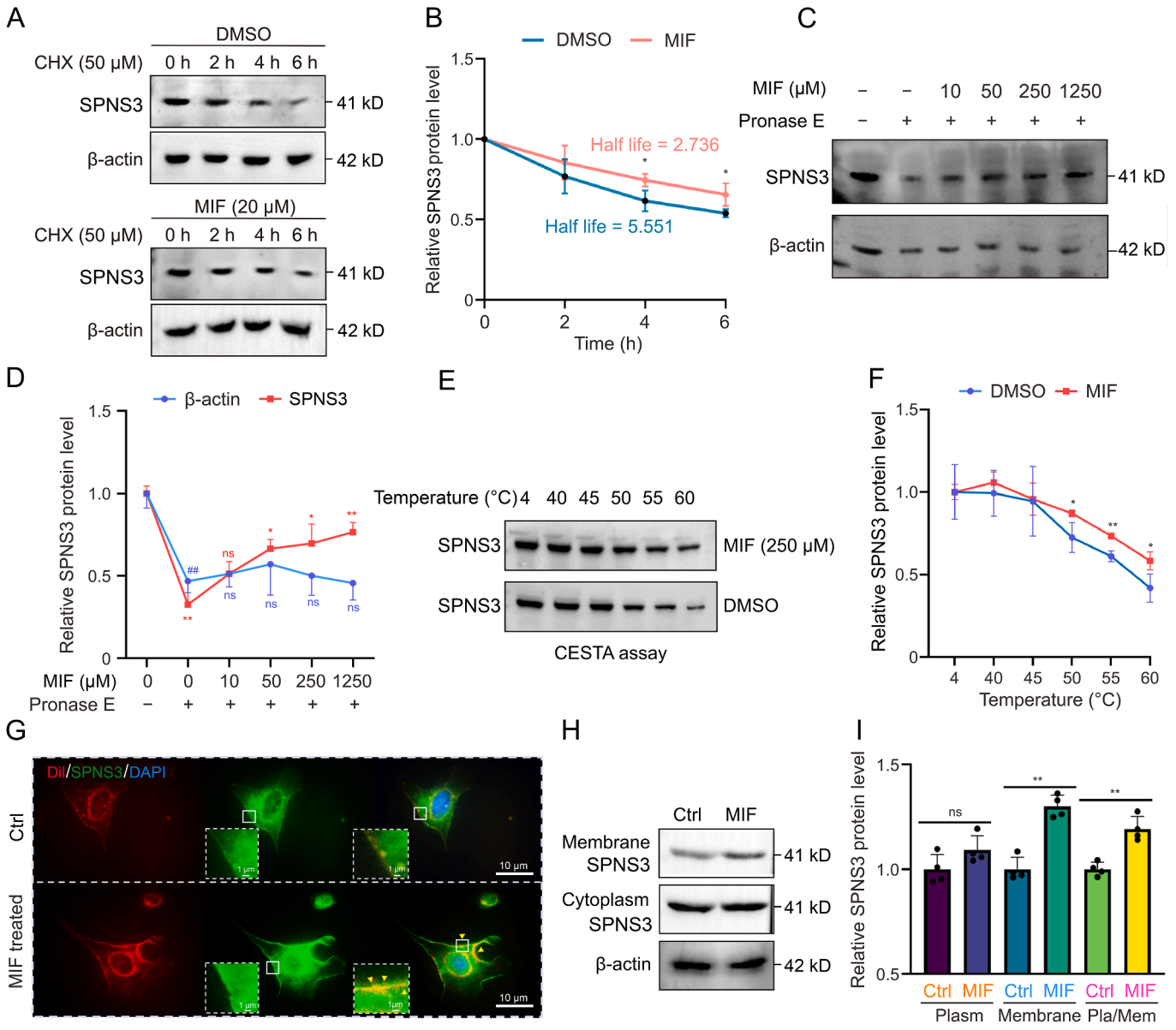
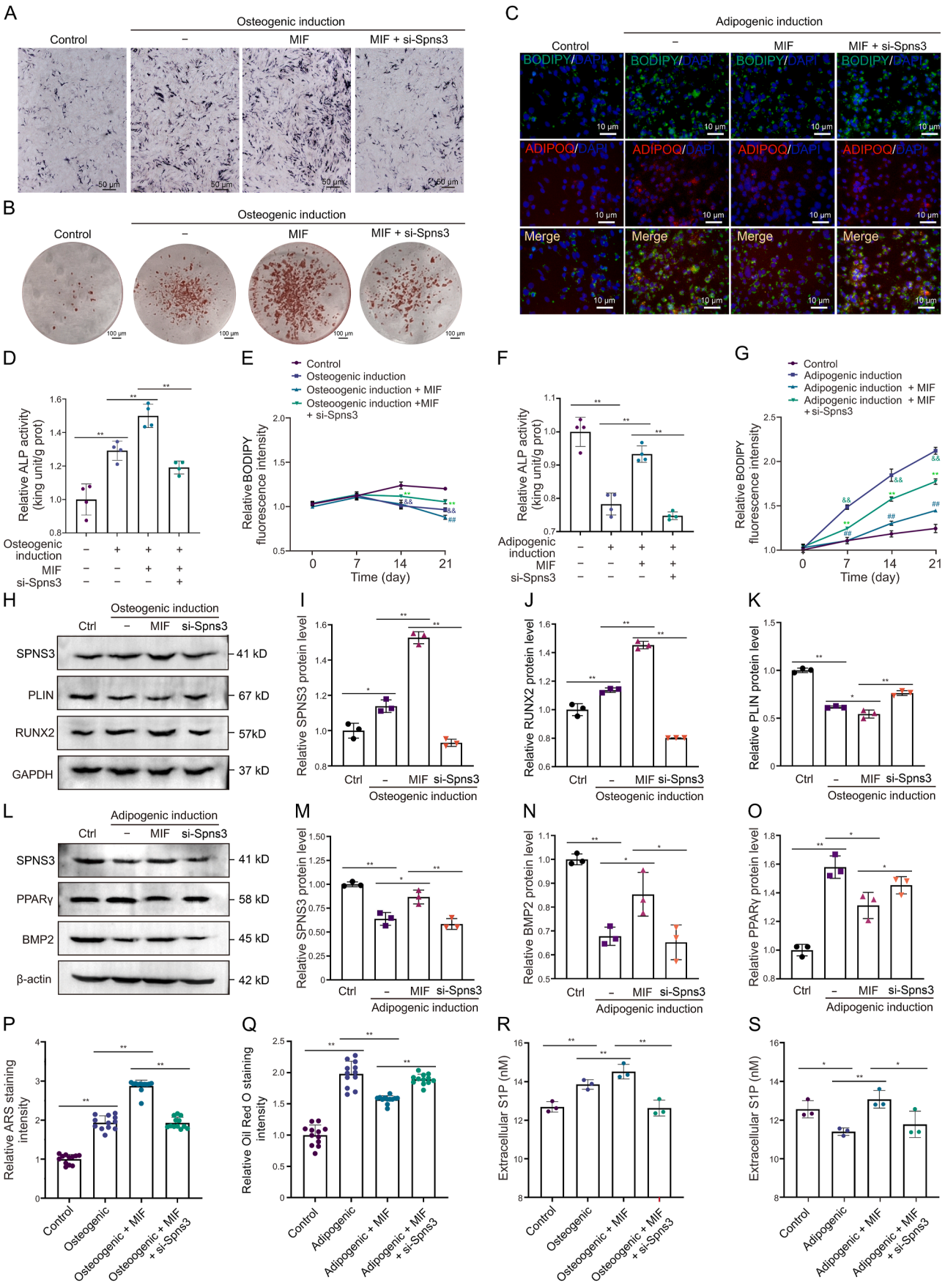


Fig. 7. Mifepristone (MIF) increased the stability and facilitated membrane localization of SPNS lysolipid transporter 3 (SPNS3). (A, B) Protein stability assays detect MIF's effect on SPNS3 via cycloheximide (CHX) treatment at the specified times (A) and quantitative analysis (B). $n = 3$, $^{*}P < 0.05$. (C, D) Protein stability assays detect MIF's effect on SPNS3 via treatment of pronase E (C) and quantitative analysis (D). $n = 3$, $^{*}P < 0.05$, $^{**}P < 0.01$; ns, not significant. (E, F) Protein stability assays detect MIF's effect on SPNS3 via cellular thermal shift assay (CETSA) (E) and quantitative analysis (F). $n = 3$, $^{*}P < 0.05$, $^{**}P < 0.01$. (G) Immunofluorescence (IF) staining indicated MIF facilitated membrane localization of SPNS3. $n = 3$. (H, I) Western blot (WB) assay (H) and quantitative analysis (I) indicated MIF facilitated membrane localization of SPNS3. $n = 3$, $^{**}P < 0.01$; ns, not significant. Ctrl: control; DMSO: dimethyl sulfoxide; Dil: 1,1′-dioctadecyl-3,3,3′,3′-tetramethylindocarbocyanine perchlorate; DAPI: 4′,6-diamidino-2-phenylindole; Ctrl: control; Pla: plasm; Mem: membrane.

visualize lipid droplets (Fig. 3I), while osteogenic activity was evaluated through ALP and ARS (Figs. 3J and K). These analyses confirmed that S1P promotes osteogenesis and suppresses adipogenesis in the BMSCs via SPNS3.

In the AAV-si-Spns3 injected mouse model, a reduction in bone mass and bone formation activity was observed (Figs. 3L–T), alongside an increase in BMAds and serum lipid levels (Figs. 3U and V). Additionally, a co-culture experiment involving BMSCs and

Fig. 6. Identifying potential therapeutic agents that target SPNS lysolipid transporter 3 (SPNS3) via the molecular docking based virtual screening technology. (A) Basal information of U.S. Food and Drug Administration (US FDA) proved small molecule drug library. (B) Top 10 obtained molecules that target SPNS3 via molecular docking based virtual screening technology. (C, D) All 10 molecules (C) were bound in the same pocket area (D). (E) Effects verification of 10 molecules on bone marrow mesenchymal stromal cells (BMSCs) differentiation tendency. $n = 4$ (independent biological replicates, the same as below). (F) Effects verification of 10 molecules on mice serum bone turnover parameters and lipid metabolism parameters. $n = 4$. (G, H) Three-dimensional (3D) (G) and two-dimensional (2D) (H) binding diagrams between mifepristone (MIF) and SPNS3 by molecular docking. (I) Mutation of 5 interacted residues. (J) Binding energy between MIF and SPNS3 after mutation. $n = 10$. (K) Structure stability of SPNS3 after mutation ($\Delta\Delta G_{pred} > 0$ means unstable mutation). (L) Root mean square deviation (RMSD) values of SPNS3-MIF complex and single molecules in 50 ns molecular dynamics simulation (MD). (M) Gibbs energy landscape diagram of MD showing the most stable point of the complex. (N, O) 3D (N) and 2D (O) binding diagrams between MIF and SPNS3 on the most stable point. ADIPOQ: adiponectin; ALP: alkaline phosphatase; ARS: Alizarin Red S; OCN: osteocalcin; OPG: osteoprotegerin; LDL-C: low-density lipoprotein; T-CHO: total cholesterol; TG: total triglyceride; OVX: ovariectomized; HFD: high fat diet; DMSO: dimethyl sulfoxide.


A
Osteogenic induction
Control
–
MIF
MIF + si-Spns3
50 μm
B
Osteogenic induction
Control
–
MIF
MIF + si-Spns3
100 μm
C
Adipogenic induction
Control
–
MIF
MIF + si-Spns3
BODIPY/DAPI
ADIPOQ/DAPI
Merge
10 μm
D
Relative ALP activity (king unit/g prot)
Osteogenic induction
MIF
si-Spns3
E
Control
Osteogenic induction
Osteoogenic induction + MIF
Osteoogenic induction +MIF + si-Spns3
Relative BODIPY fluorescence intensity
Time (day)
F
Relative ALP activity (king unit/g prot)
Adipogenic induction
MIF
si-Spns3
G
Control
Adipogenic induction
Adipogenic induction + MIF
Adipogenic induction + MIF + si-Spns3
Relative BODIPY fluorescence intensity
Time (day)
H
Osteogenic induction
Ctrl
–
MIF
si-Spns3
SPNS3
PLIN
RUNX2
GAPDH
41 kD
67 kD
57kD
37 kD
I
Relative SPNS3 protein level
Osteogenic induction
J
Relative RUNX2 protein level
Osteogenic induction
K
Relative PLIN protein level
Osteogenic induction
L
Adipogenic induction
Ctrl
–
MIF
si-Spns3
SPNS3
PPARγ
BMP2
β-actin
41 kD
58 kD
45 kD
42 kD
M
Relative SPNS3 protein level
Adipogenic induction
N
Relative BMP2 protein level
Adipogenic induction
O
Relative PPARγ protein level
Adipogenic induction
P
Relative ARS staining intensity
Control
Osteogenic
Osteogenic + MIF
Osteogenic + MIF + si-Spns3
Q
Relative Oil Red O staining intensity
Control
Adipogenic
Adipogenic + MIF
Adipogenic + MIF + si-Spns3
R
Extracellular S1P (nM)
Control
Osteogenic
Osteogenic + MIF
Osteogenic + MIF + si-Spns3
S
Extracellular S1P (nM)
Control
Adipogenic
Adipogenic + MIF
Adipogenic + MIF + si-Spns3

osteoblasts/adipocytes demonstrated the exocrine effects of S1P signaling (Figs. 3W–Y). These findings further support the critical role of S1P in modulating bone and fat metabolism through SPNS3-mediated signaling.

3.6. S1P activates S1PR1 to regulate osteogenic/adipogenic balance of BMSCs

To identify the specific receptor mediating S1P's effects in BMSCs, we analyzed the expression of S1P receptors. There are five known S1P receptors (S1PR1–5) located on cell membranes. Among them, *S1PR1* gene is prominently expressed in both bone marrow and adipose tissues (Fig. 4A). In BMSCs, osteogenic induction led to an increase in *S1*pr*1* gene expression, whereas adipogenic induction resulted in its decrease; the gene expression of other S1P receptors (*S1*pr*2–5*) remained less-affected during these differentiation processes (Figs. 4B and C). Protein levels of S1PR1 in bone tissues from elderly humans and OVX&HFD mice also exhibited a reducing trend compared to the control ones (young human or sham mice) (Figs. 4D–G). In BMSCs, silencing of *S1*pr*1* gene diminished osteogenic differentiation while enhanced adipogenic differentiation (Figs. 4H–K). Most importantly, ALP, ARS, BODIPY, and ADIPOQ IF staining assays provided definitive cellular evidence (Figs. 4L–N). The consistent results from these orthogonal techniques robustly support that S1PR1, governed by S1P, is a critical node in promoting osteogenesis while inhibiting adipogenesis.

3.7. RNA-seq assay verifies the relationship between S1PR1 signaling and BMSCs osteogenesis/adipogenesis

To elucidate the global transcriptional changes and downstream pathways governed by S1PR1 signaling, the RNA-seq assay was performed (Figs. 5 and S10). Prior to sequencing, BMSCs were pre-treated with si-S1pr1 or adipogenic induction medium (Figs. 5A, S10A and S10B). Principal component analysis (PCA) revealed clear differentiation among the samples from the three groups, demonstrating the distinct transcriptional profiles (Fig. 5B). Differential expression analysis identified 322 downregulated genes and 200 upregulated genes across the groups (Figs. 5C and D, and Table S6). Subsequent pathway enrichment analysis highlighted significant alterations in pathways associated with bone turnover, lipid metabolism, and metabolic syndrome (Figs. 5E, F, and H, and Table S7). Additionally, key downstream signaling pathways of S1PR1 were significantly enriched, including the PI3K–AKt axis, Ras signaling, PID–S1P–META axis, MAPK signaling, and ERK axis (Figs. 5G and S10C, and Table S7). These findings underscore the role of S1P-mediated S1PR1 signaling in regulating bone turnover and lipid metabolism through modulating the differentiation fate of BMSCs.

3.8. Discovery of MIF as a potential anti-OP&HLP comorbidity medicine via targeting SPNS3

The profound effects of SPNS3 on bone and lipid metabolism, as well as BMSCs differentiation, prompted us to investigate the potential therapeutic agents targeting SPNS3 for the treatment of OP&HLP comorbidity (Figs. 6 and S11). Candidate drugs were screened from the US FDA-approved drug database (Fig. 6A) using a molecular docking-based virtual screening approach. Ten drugs exhibiting the highest affinity for SPNS3 were identified (Fig. 6B), all of which bound to the same pocket region of SPNS3 (Figs. 6C and D, and S11A–J). To further validate these findings, the effects of these drugs (excluding Ergotamine and Dihydroergotamine due to policy restrictions) were tested on BMSCs to assess their effects on BMSCs differentiation (Figs. 6E and S11K–P). Additionally, their effects against OP&HLP comorbidity were evaluated in the OVX&HFD mouse model (Figs. 6F and S11R–W). The results revealed that MIF (RU486), a drug commonly used for abortion, had the most significant effects in promoting osteogenesis and inhibiting adipogenesis in BMSCs, while also demonstrating substantial anti-OP and serum lipid-lowering effects. Furthermore, MIF was found to increase the extracellular S1P levels in BMSCs (Fig. S11Q) and the serum S1P levels in OVX&HFD mice (Fig. S11X).

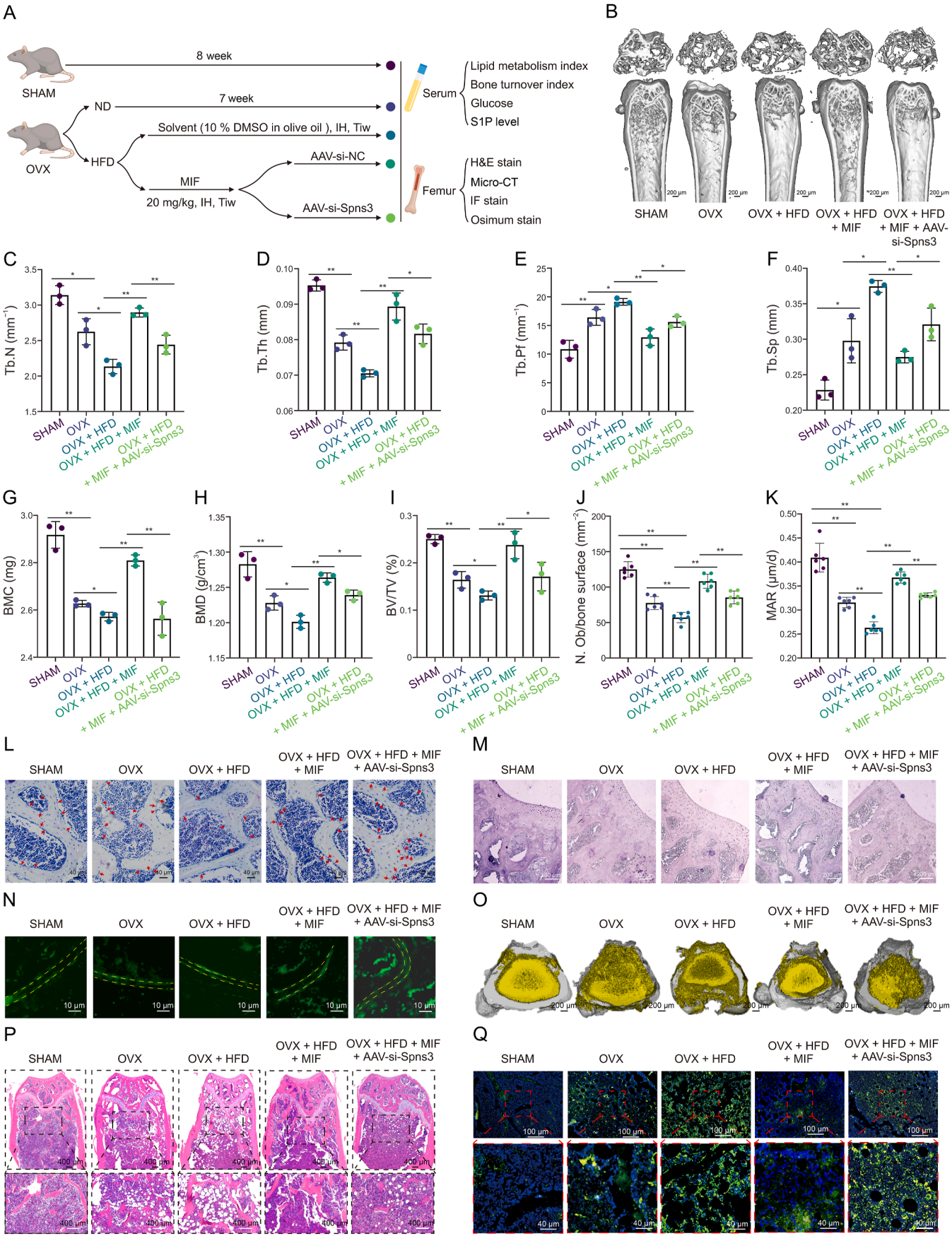
As shown in Figs. 6G and H, the molecular docking simulations revealed the interactions between MIF and SPNS3, including hydrogen bonds, π-π stacking interactions, and hydrophobic contacts. Upon mutating the amino acid residues involved in these interactions in SPNS3 (Fig. 6I), the binding energy of the MIF-SPNS3 complex was increased (Fig. 6J), and the stability of SPNS3 was notably altered (Fig. 6K). These findings suggest that MIF can enhance the stability of SPNS3. Furthermore, the interactions between MIF and S1PR1 were also analyzed through molecular docking, the result revealing low binding activity between them (Fig. S11Y), suggesting that the effects of MIF were relying on SPNS3, but not S1PR1.

To further evaluate the binding stability of MIF and SPNS3, molecular dynamics simulations were conducted. As depicted in Fig. 6L, the simulation system reached equilibrium and stability after the time of 27 ns. The RMSD values of the MIF-SPNS3 complex showed less volatility compared to SPNS3 alone, indicating that MIF enhances the stability of SPNS3. The most stable conformation of the MIF-SPNS3 complex was identified at the lowest point of Gibbs energy (Fig. 6M), with more additional interactions between MIF and SPNS3 which were highlighted in Figs. 6N and O.

3.9. MIF increases the stability and facilitates membrane localization of SPNS3

After predicting the binding activity between MIF and SPNS3, a series of experiments were conducted to investigate the effects of MIF on SPNS3. Cytotoxicity assessments in BMSCs showed that

Fig. 8. SPNS lysolipid transporter 3 (SPNS3) mediates effects of mifepristone (MIF) on differentiation tendency of bone marrow mesenchymal stromal cells (BMSCs). (A, B) Alkaline phosphatase (ALP) staining (A) and Alizarin Red S (ARS) staining (B) of BMSCs. $n = 3$ (independent biological replicates, the same as below). (C) Immunofluorescence (IF) staining of adipogenic differentiation indicator adiponectin (ADIPOQ) and Boron dipyrromethene (BODIPY) staining for detection of lipids, during adipogenic induction of BMSCs. $n = 3$. (D) ALP activity of BMSCs during osteogenic induction. $n = 4$, $^{**}P < 0.01$. (E) Relative BODIPY staining intensity of BMSCs during osteogenic induction. $n = 4$, $^{\&\&}P < 0.01$ vs. the control group, $^{\#\#}P < 0.01$ vs. the osteogenic induction group, $^{**}P < 0.01$ vs. the osteogenic induction + MIF group. (F) ALP activity of BMSCs during adipogenic induction. $n = 4$, $^{**}P < 0.01$. (G) Relative BODIPY staining intensity of BMSCs during adipogenic induction. $n = 4$, $^{\&\&}P < 0.01$ vs. the control group, $^{\#\#}P < 0.01$ vs. the adipogenic induction group, $^{**}P < 0.01$ vs. the adipogenic induction + MIF group. (H–K) Western blot (WB) assay (H) and quantitative analysis of SPNS3 (I), and osteogenic/adipogenic differentiation relative indicators runt-related transcription factor 2 (RUNX2) (J) and perilipin (PLIN) (K) after osteogenic induction. $n = 3$, $^{**}P < 0.01$, $^{*}P < 0.05$. (L–O) Western blot (WB) assay (L) and quantitative analysis of SPNS3 (M), and osteogenic/adipogenic differentiation relative indicators bone morphogenetic protein 2 (BMP2) (N) and proliferator-activated receptor gamma (PPARγ) (O) after adipogenic induction. $n = 3$, $^{**}P < 0.01$, $^{*}P < 0.05$. (P, Q) The effects of MIF on differentiation tendency were analyzed in mice primary BMSCs via ARS quantitative assay after osteogenic induction (P) and Oil Red O quantitative assay after adipogenic induction (Q). $n = 12$, $^{**}P < 0.01$. (R, S) Detection of extracellular sphingosine 1-phosphate (S1P) levels in primary BMSCs after osteogenic induction (R) and adipogenic induction (S). $n = 3$, $^{**}P < 0.01$, $^{*}P < 0.05$. Ctrl: control; DAPI: 4′,6-diamidino-2-phenylindole; GAPDH: glyceraldehyde-3-phosphate dehydrogenase.


A
SHAM
8 week
OVX
ND
7 week
HFD
Solvent (10 % DMSO in olive oil), IH, Tiw
MIF
20 mg/kg, IH, Tiw
AAV-si-NC
AAV-si-Spns3
Serum
Lipid metabolism index
Bone turnover index
Glucose
S1P level
Femur
H&E stain
Micro-CT
IF stain
Osimum stain
B
SHAM
OVX
OVX + HFD
OVX + HFD + MIF
OVX + HFD + MIF + AAV-si-Spns3
C
Tb.N (mm⁻¹)
D
Tb.Th (mm)
E
Tb.Pf (mm⁻¹)
F
Tb.Sp (mm)
G
BMC (mg)
H
BMD (g/cm³)
I
BV/TV (%)
J
N. Ob/bone surface (mm⁻²)
K
MAR (μm/d)
L
M
N
O
P
Q

MIF at concentrations below 100 μM exhibited no toxic effects (Fig. S11Z). Firstly, SPNS3 demonstrated a significantly prolonged half-life in the presence of MIF, indicating that MIF could enhance SPNS3 stability (Figs. 7A and B) by CHX chase assay. Further analysis using a pronase E enzymolysis assay (Figs. 7C and D) and a cellular thermal shift assay (CETSA; Figs. 7E and F) confirmed that MIF improved the hydrolytic and thermal stability of SPNS3. Additionally, MIF treatment enhanced the membrane localization of SPNS3 in BMSCs, as demonstrated through imaging and biochemical analyses (Figs. 7G–I). These findings suggest that MIF stabilizes SPNS3 and promotes its functional integration into the cell membrane, indirectly augmenting its biological activity.

3.10. MIF promotes the osteogenic differentiation tendency of BMSCs via SPNS3

We next assessed whether MIF's stabilization of SPNS3 translates to functional effects on BMSC differentiation (Figs. 8 and S12). ALP and ARS staining demonstrated that MIF significantly promoted osteogenic differentiation of BMSCs (Figs. 8A and B). Conversely, BODIPY staining and ADIPOQ IF staining indicated that MIF inhibited adipogenic differentiation (Fig. 8C). These effects were abrogated by knockdown of *Spns3* gene, suggesting that SPNS3 is essential for MIF's regulatory effects on BMSCs differentiation fate. Quantitative analyses using a multimode reader and WB assays during osteogenic induction (Figs. 8D, E, and H–K) and adipogenic induction (Figs. 8F, G, and L–O) further confirmed these findings. In primary BMSCs isolated from the femurs of healthy mice, MIF consistently demonstrated regulatory effects on the differentiation fate (Figs. 8P and Q), and extracellular S1P levels were significantly increased following MIF stimulation (Figs. 8R and S). Moreover, the effects of MIF on BMSCs were also inhibited by the knockdown of *S1pr1* gene (Fig. S12). This result further supports the conclusion that MIF exerts its effects through the SPNS3–S1P–S1PR1 signaling axis.

3.11. MIF exhibits anti-bone loss effects in OP&HLP comorbidity mice

The *in vivo* therapeutic efficacy of MIF against OP&HLP comorbidity was evaluated using a mouse model subjected to OVX and HFD induction (Fig. 9). The flowchart of mice experiment is shown in Fig. 9A. Micro-CT analysis of femurs from the OVX&HFD mouse model revealed significantly more severe bone loss compared to the OVX mice and control mice. Notably, MIF treatment mitigated OVX&HFD induced bone loss, which was abolished by AAV-si-Spns3 injection (Figs. 9B–I). Further assessments of bone formation supported the efficacy of MIF: demonstrated by the improved number of osteoblasts on trabecular bone surfaces (Figs. 9J and L), increased ALP activity in femoral bone tissue (Fig. 9M), and the accelerated bone deposition rate measured by calcein double labeling (Figs. 9K and N). These effects were reversed upon *Spns3* gene knockdown, further confirming SPNS3's critical role in MIF's actions.

MIF's impact on adipose tissue was also evaluated. Osmium ion labeling (Fig. 9O), H&E staining (Fig. 9P, showing circular cavities left by adipose tissue in cancellous bone), and immunofluorescence staining for PLIN, a critical adipocyte marker (Fig. 9Q), collectively indicated that MIF effectively inhibited adipose tissue accumulation in the bone marrow of OVX + HFD mice. The anti-adipogenic effect was also blocked by *Spns3* gene knockdown, underscoring the importance of the SPNS3 axis in mediating MIF's effects on increasing bone deposition and decreasing adipose formation.

3.12. MIF influences bone turnover and lipid metabolism related indicators

Subsequent investigations focused on bone turnover and lipid metabolism markers in mouse models to further elucidate MIF's effects (Figs. S13 and S14). WB assays demonstrated MIF's ability to enhance osteogenic differentiation while suppressing adipogenic differentiation through targeting SPNS3 (Figs. S14A–H). These findings were corroborated by changes in liver-to-body weight ratios and serum S1P levels (Figs. S13A, S13B, S14I, and S14J), as well as alterations in the key indicators of bone turnover and lipid metabolism (Figs. S14L–T).

Interestingly, MIF treatment also normalized the abnormal serum glucose levels induced by OVX&HFD (Figs. S13E and S14K). Furthermore, the elevated serum glucocorticoid levels observed in OVX + HFD mice were significantly reduced following MIF administration (Figs. S13C and D). These results suggest that MIF not only improves bone health and lipid metabolism but also exerts beneficial effects on metabolic syndrome.

3.13. MIF treated mice serum facilitates osteogenic differentiation and MIF treated BMSCs facilitate repairment of calvarial bone defect via SPNS3

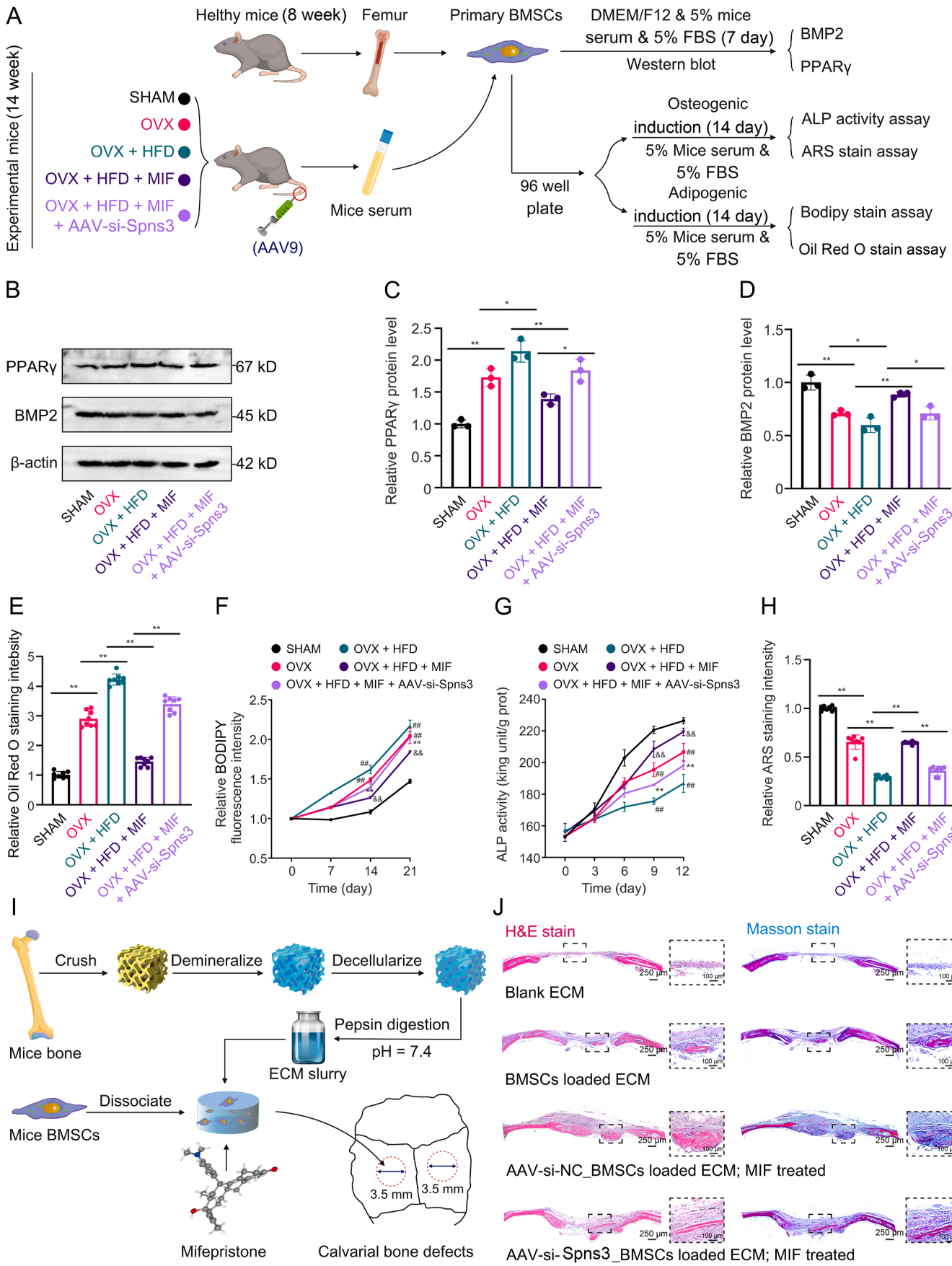
Finally, to explore the translational potential of MIF's effects, we investigated whether the effects of MIF could be transmitted via serum. Serum samples were collected from mice under various treatments and used to culture mouse BMSCs (Fig. 10A). To eliminate residual MIF in the serum, samples were obtained five days after the last injection of MIF. As illustrated in Figs. 10B–H, serum from MIF-treated mice significantly promoted osteogenic differentiation and suppressed adipogenic differentiation of BMSCs compared with serum from OVX&HFD mice. These effects, however, were abrogated in serum from mice injected with AAV-si-Spns3, highlighting the critical role of SPNS3 in mediating MIF's effects.

Additionally, a calvarial bone defect model was employed to evaluate MIF's role in bone repair (Fig. 10I). BMSCs treated with or without MIF were embedded in an extracellular matrix (ECM) and applied to the defect sites. MIF-treated BMSCs exhibited enhanced bone and collagen formation at the defect areas, while silencing *Spns3* gene inhibited these regenerative effects (Fig. 10J). These findings further underscore the therapeutic potential of MIF in bone regeneration through the SPNS3 pathway.

4. Discussion

In aging female OP and PMOP patients, estrogen deficiency often coexists with obesity, creating a complex clinical phenotype

Fig. 9. *In vivo* effect studies of mifepristone (MIF) on ovariectomized + high fat diet (OVX&HFD) induced bone loss. (A) Flowchart of mice experiments. (B–I) Micro computed tomography (micro-CT) assay of mice femurs (B) and bone mass related parameters: trabecular number (Tb. N) (C), trabecular thickness (Tb. Th) (D), trabecular pattern factor (Tb. Pf) (E), trabecular separation (Tb. Sp) (F), bone mineral content (BMC) (G), bone mineral density (BMD) (H), and bone volume/tissue volume (BV/TV) (I). $n = 3$, $^{**}P < 0.01$, $^{*}P < 0.05$ (independent biological replicates, the same as below). (J) Quantitative analysis of osteoblasts. $n = 6$, $^{**}P < 0.01$. (K) Quantitative analysis of mineral apposition rate (MAR). $n = 6$, $^{**}P < 0.01$. (L) Toluidine blue staining for osteoblast calculating. $n = 6$. (M) Alkaline phosphatase (ALP) staining of mice femur. $n = 3$. (N) Calcein labeled new bone deposits for quantitative analysis of MAR. $n = 6$. (O) Osmium ion staining for femur fat tissues assay by micro-CT. $n = 3$. (P) Hematoxylin-eosin (H&E) staining of mice femur. $n = 3$. (Q) Immunofluorescence (IF) staining for detection of perilipin (PLIN). $n = 3$. SHAM: sham-operated; OVX: ovariectomized; ND: normal diet; HFD: high fat diet; S1P: sphingosine 1-phosphate; MIF: mifepristone; N. Ob: number of osteoblasts; AAV: adeno-associated virus.


A
Experimental mice (14 week)
SHAM
OVX
OVX + HFD
OVX + HFD + MIF
OVX + HFD + MIF + AAV-si-Spns3
(AAV9)
Helthy mice (8 week)
Femur
Primary BMSCs
Mice serum
DMEM/F12 & 5% mice serum & 5% FBS (7 day)
Western blot
BMP2
PPARγ
96 well plate
Osteogenic induction (14 day)
5% Mice serum & 5% FBS
ALP activity assay
ARS stain assay
Adipogenic induction (14 day)
5% Mice serum & 5% FBS
Bodipy stain assay
Oil Red O stain assay
B
PPARγ
BMP2
β-actin
67 kD
45 kD
42 kD
C
Relative PPARγ protein level
D
Relative BMP2 protein level
E
Relative Oil Red O staining intebsity
F
Relative BODIPY fluorescence intensity
Time (day)
G
ALP activity (king unit/g prot)
Time (day)
H
Relative ARS staining intensity
I
Crush
Demineralize
Decellularize
Mice bone
Pepsin digestion
pH = 7.4
ECM slurry
Dissociate
Mice BMSCs
Mifepristone
3.5 mm
3.5 mm
Calvarial bone defects
J
H&E stain
Masson stain
Blank ECM
BMSCs loaded ECM
AAV-si-NC_BMSCs loaded ECM; MIF treated
AAV-si-Spns3_BMSCs loaded ECM; MIF treated

whose combined impact on bone metabolism remains incompletely understood. While OVX and HFD are standard approaches to establish independent models for OP and metabolic dysfunction, respectively [14], few studies have utilized the combined OVX&HFD model to investigate OP&HLP comorbidity. Our development of this model successfully simulated the dual abnormalities of bone and lipid metabolism, demonstrating more severe bone loss and higher serum lipid levels compared to the traditional OVX model. Notably, the observed disturbances in blood glucose and glucocorticoid levels suggest this model recapitulates aspects of metabolic syndrome characterized by OP&HLP coexistence. This is particularly relevant given the established links between metabolic syndrome and disorders of bone/lipid metabolism. Interestingly, MIF, previously proposed as a preventive agent against metabolic syndrome [29], not only exhibited anti-OP and anti-HLP effects in our experiments but also ameliorated abnormal glucose and glucocorticoid levels, underscoring its potential for addressing metabolic syndrome and its skeletal complications.

Our comprehensive approach combining bioinformatics with experimental validation identified SPNS3 and POU2F2 as key players in OP&HLP pathogenesis. While SPNS3, an SPNS family member, is recognized for its S1P transport function [36] and has limited reported associations with leukemia [36], its broader disease relevance and structural characteristics remain largely unexplored. Our findings of its high bone marrow expression and positive correlation with bone formation suggest a previously unrecognized critical role in bone metabolism, potentially linking its S1P transport capability to osteogenesis and lipid regulation. This represents a significant expansion of SPNS3's functional repertoire beyond its previously limited disease associations.

In contrast to the tissue-restricted expression of SPNS3, POU2F2 is ubiquitously expressed with no specific bone tissue localization detected in our study. Although well-established as a transcription factor involved in various cancers [37], no prior evidence connected POU2F2 to OP pathogenesis. Our demonstration that POU2F2 transcriptionally activates SPNS3 establishes not only a novel regulatory relationship but also reveals POU2F2's previously unknown role in bone metabolism, as evidenced by impaired osteogenic differentiation following *Pou2f2* gene knockdown. This discovery is particularly significant given the current lack of therapeutic options targeting POU2F2 due to its structural simplicity and absence of a druggable pocket [38]. Conversely, SPNS3's complex channel architecture presents a more feasible drug target [39], positioning it as the more promising therapeutic node within this newly identified pathway.

The connection between SPNS3 and OP&HLP comorbidity led us to investigate S1P-mediated signaling. S1P, a ubiquitous bioactive lipid with established roles in immunity, allergy, cancer, and bone remodeling [34,40], displayed significantly reduced levels in OVX&HFD mice and elderly women, consistent with previous findings [21]. S1P supplementation enhanced BMSC osteogenesis, supporting its critical bone-forming role. Importantly, our co-culture and serum induction experiments revealed that S1P exerts its anti-OP and anti-HLP effects through autocrine, paracrine, and endocrine mechanisms, highlighting its multifaceted regulatory capacity in bone-fat crosstalk.

S1P signaling requires activation of its membrane receptors (S1PR1–5) [41], among which S1PR1 shows predominant expression in bone and adipose tissues with established bone metabolic functions [42]. Our finding that *S1*p*r1* gene knockdown promoted adipogenesis while suppressing osteogenesis in BMSCs further solidifies its regulatory role. RNA-seq analysis confirmed that *S1*p*r1* gene knockdown significantly affected key pathways including MAPK and PI3K-AKt, along with downstream effectors like ERKs, Ras, and Rac, all associated with bone turnover and lipid metabolism. These results collectively highlight the fundamental importance of the SPNS3–S1P–S1PR1 axis in OP&HLP comorbidity.

The strategic advantages of drug repurposing—including shorter development cycles, reduced costs, and higher success rates [43]—led us to explore existing drugs targeting this axis. While recent studies have investigated MIF's potential against HLP and metabolic syndrome [29], with evidence showing reduced adipocyte differentiation in 3T3-L1 cells [44] and enhanced osteochondral differentiation in human MSCs [45], no research has directly demonstrated anti-OP effects. Our identification of MIF as a SPNS3 binder through US FDA-approved drug screening, supported by molecular docking, dynamics simulations, and experimental validation of SPNS3 stabilization, reveals a novel mechanism of action. The comprehensive *in vitro* and *in vivo* demonstration of MIF's efficacy against OP&HLP comorbidity via SPNS3 targeting provides compelling evidence for therapeutic repurposing. Importantly, the dramatic decline of progesterone receptors (PR) in postmenopausal women [46] may serendipitously avoid potential PR-mediated side effects of MIF in PMOP patients. Additionally, since excessive glucocorticoid contributes to OP [47] and high-dose MIF antagonizes glucocorticoid receptors [48], future studies should explore the therapeutic potential of optimized MIF dosing regimens for OP treatment.

Our findings on the POU2F2–SPNS3–S1P–S1PR1 axis should be viewed in the context of emerging multi-omics insights into bone-fat crosstalk. While recent studies have revealed complex molecular networks in bone-lipid interactions through integrated transcriptomic and proteomic approaches [49], our work uniquely identifies SPNS3 as a previously overlooked regulator in bone biology. Unlike its homolog SPNS2, SPNS3 demonstrates bone marrow-specific expression and functionally governs BMSC fate determination through S1P transport—a role not previously described in OP pathogenesis. This mechanistic understanding of SPNS3's function in bone metabolism represents a significant advance beyond its previously limited association with hematopoietic malignancies [36], positioning it as a compelling therapeutic target within the broader landscape of skeletal metabolism research.

In conclusion, utilizing a novel OVX&HFD-induced comorbidity mouse model, we have delineated the important role of the POU2F2–SPNS3–S1P–S1PR1 signaling axis in regulating BMSC differentiation and bone/lipid metabolism. Our findings establish SPNS3 as a transcriptional target of POU2F2 and identify the US FDA-approved drug MIF as a SPNS3-binding agent that stabilizes

Fig. 10. Mifepristone (MIF) treated mice serum facilitates osteogenic differentiation and MIF treated bone marrow mesenchymal stromal cells (BMSCs) facilitate repair of calvarial bone defect via SPNS lysolipid transporter 3 (SPNS3). (A) Flowchart of mice serum related experiments. (B–D) Western blot (WB) assay (B) and quantitative analysis of adipogenic related peroxisome proliferator-activated receptor gamma (PPARγ) (C) and osteogenic related bone morphogenetic protein 2 (BMP2) (D). $n = 3$, $^{**}P < 0.01$, $^{*}P < 0.05$ (independent biological replicates, the same as below). (E) Quantitative analysis of adipogenic related Oil Red O staining. $n = 8$, $^{**}P < 0.01$. (F) Quantitative analysis of Boron dipyrromethene (BODIPY) staining. $n = 8$, $^{\#\#}P < 0.01$ vs. the SHAM group, $^{\&\&}P < 0.01$ vs. the OVX + HFD group, $^{**}P < 0.01$ vs. the OVX + HFD + MIF group. (G) Quantitative analysis of alkaline phosphatase (ALP) staining. $n = 8$, $^{\#\#}P < 0.01$ vs. the SHAM group, $^{\&\&}P < 0.01$ vs. the OVX + HFD group, $^{**}P < 0.01$ vs. the OVX + HFD + MIF group. (H) Quantitative analysis of Alizarin Red S (ARS) staining. $n = 8$, $^{**}P < 0.01$. (I) Flowchart of calvarial bone defect experiment. (J) Hematoxylin-eosin (H&E) staining for revealing newly formed bone tissue and Masson's trichrome staining for revealing newly formed collagen among the defect area. ECM: extracellular matrix; SHAM: sham-operated; OVX: ovariectomized; HFD: high fat diet; AAV: adeno-associated virus; DMEM/F12: dulbecco's modified eagle medium/nutrient mixture F-12; FBS: fetal bovine serum.

the protein and promotes osteogenesis. These results advance our mechanistic understanding of OP&HLP comorbidity and highlight the therapeutic potential of targeting the SPNS3–S1P axis.

CRediT authorship contribution statement

Hao Li: Writing – review & editing, Writing – original draft, Validation, Data curation, Conceptualization. **Wanyu Sang:** Methodology, Investigation, Formal analysis, Data curation. **Sihang Fan:** Software, Data curation. **Changyuan Wang:** Validation, Software, Data curation. **Lu Liu:** Visualization, Validation, Software. **Shan Wang:** Methodology, Formal analysis. **Mozhen Liu:** Supervision, Investigation. **Huijun Sun:** Validation, Project administration, Funding acquisition.

Data availability

Publicly available datasets were analyzed in this study and can be accessed via the GEO database under the following accession numbers: GSE68303, GSE194075, GSE218105, GSE35959, and GSE230665. Additionally, the raw sequencing data generated in this research have been deposited in the GEO database (Accession Number: GSE299908).

Declaration of competing interest

The authors declare that they have no known competing financial interests or personal relationships that could have appeared to influence the work reported in this paper.

Acknowledgments

This study was partially supported by the National Natural Science Foundation of China (Grant No.: 82073851), Fund of the Department of Education of Liaoning Province (Grant No.: LJ232410161020), and the Medical Peak Program of Dalian (Grant No.: DF2023007).

Appendix A. Supplementary data

Supplementary data to this article can be found online at https://doi.org/10.1016/j.jpha.2026.101608.

References

[1] F. Pouresmaeili, B. Kamali Dehghan, M. Kamarehei, et al., A comprehensive overview on osteoporosis and its risk factors, Therapeut. Clin. Risk Manag. 14 (2018) 2029–2049.
[2] X. Zhu, W. Bai, H. Zheng, Twelve years of GWAS discoveries for osteoporosis and related traits: advances, challenges and applications, Bone Res. 9 (2021), 23.
[3] C. Cooper, G. Campion, L.J. Melton, Hip fractures in the elderly: a world-wide projection, Osteoporos. Int. 2 (1992) 285–289.
[4] J. Li, X. Chen, L. Lu, et al., The relationship between bone marrow adipose tissue and bone metabolism in postmenopausal osteoporosis, Cytokine Growth Factor Rev. 52 (2020) 88–98.
[5] L. Tian, X. Yu, Lipid metabolism disorders and bone dysfunction-interrelated and mutually regulated (Review), Mol. Med. Rep. 12 (2015) 783–794.
[6] S.H. Ko, H.S. Kim, Menopause-associated lipid metabolic disorders and foods beneficial for postmenopausal women, Nutrients 12 (2020), 202.
[7] J. Paccou, S. Badr, D. Lombardo, et al., Bone marrow adiposity and fragility fractures in postmenopausal women: the ADIMOS case-control study, J. Clin. Endocrinol. Metab. 108 (2023) 2526–2536.
[8] F. Pirih, J. Lu, F. Ye, et al., Adverse effects of hyperlipidemia on bone regeneration and strength, J. Bone Miner. Res. 27 (2012) 309–318.
[9] S. Karr, Epidemiology and management of hyperlipidemia, Am. J. Manag. Care 23 (2017) S139–S148.
[10] W. Yin, Z. Li, W. Zhang, Modulation of bone and marrow niche by cholesterol, Nutrients 11 (2019), 1394.
[11] Y. Tintut, S. Morony, L.L. Demer, Hyperlipidemia promotes osteoclastic potential of bone marrow cells *ex vivo*, Arterioscler. Thromb. Vasc. Biol. 24 (2004) e6–e10.
[12] H. Ren, K. Mao, X. Yuan, et al., AN698/40746067 suppresses bone marrow adiposity to ameliorate hyperlipidemia-induced osteoporosis through targeted inhibition of ENTR1, Biomed. Pharmacother. 176 (2024), 116843.
[13] M. Tencerova, M. Kassem, The bone marrow-derived stromal cells: commitment and regulation of adipogenesis, Front. Endocrinol. 7 (2016), 127.
[14] D. Ali, F. Figeac, A. Caci, et al., High-fat diet-induced obesity augments the deleterious effects of estrogen deficiency on bone: evidence from ovariectomized mice, Aging Cell 21 (2022), e13726.
[15] B. Yu, L. Huo, Y. Liu, et al., PGC-1α controls skeletal stem cell fate and bone-fat balance in osteoporosis and skeletal aging by inducing TAZ, Cell Stem Cell 23 (2018) 193–209.
[16] D. Kim, W. Tian, T.T. Wu, et al., Abnormal lymphatic sphingosine-1-phosphate signaling aggravates lymphatic dysfunction and tissue inflammation, Circulation 148 (2023) 1231–1249.
[17] A.H. Janneh, C. Atkinson, S. Tomlinson, et al., Sphingolipid metabolism and complement signaling in cancer progression, Trends Cancer 9 (2023) 782–787.
[18] S.H. Lee, S.Y. Lee, Y.S. Lee, et al., Higher circulating sphingosine 1-phosphate levels are associated with lower bone mineral density and higher bone resorption marker in humans, J. Clin. Endocrinol. Metab. 97 (2012) E1421–E1428.
[19] A. Meshcheryakova, D. Mechtcheriakova, P. Pietschmann, Sphingosine 1-phosphate signaling in bone remodeling: multifaceted roles and therapeutic potential, Expert Opin. Ther. Targets 21 (2017) 725–737.
[20] M.M. Ardawi, A.A. Rouzi, N.S. Al-Senani, et al., High plasma sphingosine 1-phosphate levels predict osteoporotic fractures in postmenopausal women: the center of excellence for osteoporosis research study, J. Bone Metab. 25 (2018) 87–98.
[21] S. Weske, M. Vaidya, A. Reese, et al., Targeting sphingosine-1-phosphate lyase as an anabolic therapy for bone loss, Nat. Med. 24 (2018) 667–678.
[22] T. An, J. Hao, S. Sun, et al., Efficacy of statins for osteoporosis: a systematic review and meta-analysis, Osteoporos. Int. 28 (2017) 47–57.
[23] A. Oryan, A. Kamali, A. Moshiri, Potential mechanisms and applications of statins on osteogenesis: current modalities, conflicts and future directions, J. Contr. Release 215 (2015) 12–24.
[24] M. Leutner, C. Matzhold, L. Bellach, et al., Diagnosis of osteoporosis in statin-treated patients is dose-dependent, Ann. Rheum. Dis. 78 (2019) 1706–1711.
[25] M. Leutner, M. Butylina, C. Matzhold, et al., Simvastatin therapy in higher dosages deteriorates bone quality, Biomed. Pharmacother. 158 (2023), 114089.
[26] T. Hayashi, K. Ina, M. Maeda, et al., The effects of selective estrogen receptor modulator treatment following hormone replacement therapy on elderly postmenopausal women with osteoporosis, Nitric Oxide 24 (2011) 199–203.
[27] L. Koch, Risk of endometrial cancer with combined estradiol–progestin therapy in postmenopausal women, Nat. Rev. Endocrinol. 6 (2010), 121.
[28] J. Duan, H. Li, C. Wang, et al., BMSC-derived extracellular vesicles promoted osteogenesis via Axin2 inhibition by delivering miR-16-5p, Int. Immunopharmacol. 120 (2023), 110319.
[29] F. Díaz-Castro, M. Monsalves-Álvarez, L.E. Rojo, et al., Mifepristone for treatment of metabolic syndrome: beyond Cushing's syndrome, Front. Pharmacol. 11 (2020), 429.
[30] T.H. Yu, T.T. Yeh, C. Su, et al., Preparation and characterization of extracellular matrix hydrogels derived from acellular cartilage tissue, J. Funct. Biomater. 13 (2022) 279–285.
[31] W. Chen, Q. Yang, L. Hu, et al., Shared diagnostic genes and potential mechanism between PCOS and recurrent implantation failure revealed by integrated transcriptomic analysis and machine learning, Front. Immunol. 14 (2023), 1175384.
[32] J. Li, G. Wang, X. Xv, et al., Identification of immune-associated genes in diagnosing osteoarthritis with metabolic syndrome by integrated bioinformatics analysis and machine learning, Front. Immunol. 14 (2023), 1134412.
[33] R. Ieva, R.-P. Rafael, B.-M. Romain, et al., JASPAR 2024: 20th anniversary of the open-access database of transcription factor binding profiles, Nucleic Acids Res. 14 (2023) D174–D182.
[34] T. Nishi, N. Kobayashi, Y. Hisano, et al., Molecular and physiological functions of sphingosine 1-phosphate transporters, Biochim. Biophys. Acta BBA Mol. Cell Biol. Lipds. 1841 (2014) 759–765.
[35] R. Dastvan, A. Rasouli, S. Dehghani-Ghahnaviyeh, et al., Proton-driven alternating access in a spinster lipid transporter, Nat. Commun. 13 (2022), 5161.
[36] Y. Hong, X. Tian, M. Wang, et al., Bioinformatics-based identification of SPNS3 (Spinster homolog 3) as a prognostic biomarker of apoptosis resistance in acute myeloid leukemia, Bioengineered 12 (2021) 7837–7848.
[37] S. Wang, J. Tie, W. Wang, et al., POU2F2-oriented network promotes human gastric cancer metastasis, Gut 65 (2016) 1427–1438.
[38] A. Chen, A.N. Koehler, Transcription factor inhibition: lessons learned and emerging targets, Trends Mol. Med. 26 (2020) 508–518.
[39] H. Li, X. Sun, W. Cui, et al., Computational drug development for membrane protein targets, Nat. Biotechnol. 42 (2024) 229–242.
[40] S. Spiegel, S. Milstien, The outs and the ins of sphingosine-1-phosphate in immunity, Nat. Rev. Immunol. 11 (2011) 403–415.
[41] H. Yu, Targeting S1PRs as a therapeutic strategy for inflammatory bone loss diseases: beyond regulating S1P signaling, Int. J. Mol. Sci. 22 (2021) 4411–4418.

[42] X. Xu, Y. Han, T. Zhu, et al., The role of SphK/S1P/S1PR signaling pathway in bone metabolism, Biomed. Pharmacother. 169 (2023), 115838.
[43] S. Pushpakom, F. Iorio, P.A. Eyers, et al., Drug repurposing: progress, challenges and recommendations, Nat. Rev. Drug Discov. 18 (2019) 41–58.
[44] T. Hashimoto, K. Hirano, Effects of mifepristone on adipocyte differentiation in mouse 3T3-L1 cells, Cell. Mol. Biol. Lett. 29 (2024), 45.
[45] Y. Yu, N. Wei, C. Stanford, et al., In vitro effects of RU486 on proliferation and differentiation capabilities of human bone marrow mesenchymal stromal cells, Steroids 77 (2012) 132–137.
[46] D.E. Meza-Muñoz, M.E. Fajardo, E.L. Pérez-Luque, et al., Factors associated with estrogen receptors-α (ER-α) and-β (ER-β) and progesterone receptor abundance in obese and non obese pre- and post-menopausal women, Steroids 71 (2006) 498–503.
[47] L. Buckley, M.B. Humphrey, Glucocorticoid-induced osteoporosis, N. Engl. J. Med. 379 (2018) 2547–2556.
[48] P. Ma, Y. Zhang, Q. Liang, et al., Mifepristone (RU486) inhibits dietary lipid digestion by antagonizing the role of glucocorticoid receptor on lipase transcription, iScience 24 (2021), 102507.
[49] H. Xiao, W. Li, Y. Qin, et al., Crosstalk between lipid metabolism and bone homeostasis: exploring intricate signaling relationships, Research 7 (2024), 447.